

Shaping Asteroid Models Using Genetic Evolution (SAGE)

P. Bartczak, G. Dudziński

Astronomical Observatory Institute, Faculty of Physics, Adam Mickiewicz University, Stoleczna 36, 60-286 Poznań, Poland

22 April 2019

ABSTRACT

In this work we present SAGE (Shaping Asteroid models using Genetic Evolution) asteroid modelling algorithm based solely on photometric lightcurve data. It produces non-convex shapes, rotation axes orientations and rotational periods of asteroids. The main concept behind a genetic evolution algorithm is to produce random populations of shapes and spin axis orientations by mutating a seed shape and iterating the process until it converges to a stable global minimum. To test SAGE we have performed tests on five artificial shapes. We have also modelled (433) Eros and (9) Metis asteroids, as ground truth observations for them exist, allowing us to validate the models. We have compared derived Eros shape with NEAR Shoemaker model and Metis shape with adaptive optics and stellar occultation observations as with other available Metis models from various inversion methods.

Key words: Minor planets, asteroids, Methods: numerical, Techniques: photometric, lightcurve inversion

1 INTRODUCTION

Asteroid shapes were unknown until 1991. That year Galileo spacecraft took flyby photos of (951) Gaspra, and (243) Ida two years later. Images revealed shapes and topographic features of these two objects – far from spherical and dotted with impact craters. One cannot say though that insight into asteroids’ physical properties prior to Galileo mission had been void, as some methods of acquiring information about Solar System’s small bodies from ground-based data were already being developed.

Until this day photometry remains the main source of information about shapes, rotational states and physical properties of asteroids. Studying their lightcurves can lead to the creation of models that explain observations, at least to some extent and with some assumptions.

First thorough analysis of the lightcurve inversion problem was done by Russell (1906). His conclusions were rather pessimistic – from lightcurves one can only deduce a spin axis orientation; unambiguous determination of shape is beyond the grasp of analytical methods and any shape can be mimicked by albedo variations on a body’s surface. However, Russell’s study dealt only with zero-phase angles and geometric “scattering law”.

Nonetheless, some methods were introduced later, mainly to calculate spin axes of asteroids. The magnitude-amplitude and epoch approach (Magnusson et al. (1989), Michalowski (1993)) assumed body’s homogeneous albedo and triaxial ellipsoid shape. Given many apparitions providing different aspect angles it is possible to determine the

spin axis orientation and triaxial ellipsoid’s axis ratios a/b and b/c .

Increased computer power available to researchers led to the development of numerical methods (e.g. Uchida & Goguen (1987), Karttunen & Bowell (1989)) whose biggest achievement was representing asteroids’ models by small surface elements, enabling the application of arbitrary scattering laws. The spin axis orientation and ellipsoid axes were iteratively changed to provide the best fit to available lightcurves. Some numerical methods went beyond the simple triaxial ellipsoid model (Cellino et al. 1987) merging eight different ellipsoids into one shape.

A new lightcurve inversion method was introduced by Kaasalainen & Torppa (2001) and Kaasalainen et al. (2001). It allows to produce asteroids’ shape models, rotational periods and spin axis orientations, the only constrain on asteroid’s shape being its convexity. The resulting model is a convex hull containing shape of an asteroid. Lightcurves must be obtained from multiple apparitions in order to provide a unique solution.

Nonetheless spacecraft missions revealed that asteroids’ shapes are far more complex than simple geometric shapes and are non-convex in general. A growing number of adaptive optics and stellar occultation observations encourages to include them in the modelling process. An attempt to combine lightcurve inversion with Adaptive Optics and stellar occultations KOALA (Knitted Occultation, Adaptive optics and Lightcurve Analysis) was presented in Carry et al. (2010), where it was used to model (2) Pallas. This method has been developed further to include more observational

arXiv:1904.08940v1 [astro-ph.EP] 18 Apr 2019

techniques (Kaasalainen et al. 2011; Carry et al. 2012). Another method combining various types of data, ADAM (All-Data Asteroid Modelling algorithm), was described in Viikinkoski et al. (2015).

In this work we introduce SAGE (Shaping Asteroids with Genetic Evolution) method of modelling asteroids' shapes, spin axis orientations and period determination. In this approach only lightcurve data is used to produce non-convex shapes of asteroids, assuming a homogeneous albedo and mass distribution of a body and rotation about a single axis. Each model produced by SAGE is a physical one, i.e. the rotation axis always lies along model's greatest moment of inertia axis and goes through its centre of mass.

In section 2 we explain the concept behind a genetic evolution algorithm and describe the modelling process. In order to validate the method we have performed numerical tests on artificial test models (section 3). We have also successfully modelled (433) Eros and (9) Metis (section 4) for which *in situ* observations (for Eros), adaptive optics and stellar occultation (for Metis) exist allowing us to validate the results.

2 METHOD

2.1 Shape representation

An asteroid shape model is represented by a mesh of vertices in 3D space with triangular faces. Each face is defined as a list of three vertices in the counter-clockwise order which defines a surface normal vector direction. In SAGE 242 vertices are used to describe a shape and their positions in space are free parameters in the inversion process. To lower the degrees of freedom, every vertex lies along a ray oriented in a fixed direction. Rays are evenly distributed on a sphere. By allowing a vertex to move only along a ray its position is reduced to a single variable and a redefinition of faces is not needed when changes to the shape are made.

A more detailed model is used for lightcurve calculation. 242 parameter mesh is refined by Catmull-Clark surface subdivision algorithm (Catmull & Clark 1978) for surfaces smoothing (Fig. 1). The resulting asteroid shape model consists of 3842 vertices and 7680 faces. Only the smoothed model is used for lightcurve generation and is considered an asteroid's shape.

The choice of 242 shape parameters is dictated by several factors. We took the largest possible platonic solid, an icosahedron, with 20 congruent regular triangular faces and with each of 12 vertices being a meeting point for the same number (i.e. 5) of facets. Then, we applied consecutive Catmull-Clark surface subdivisions to get shapes with a larger number of vertices and with a distribution of face sizes as uniform as possible. The resulting solids have 62, 242, 962, 3842, . . . , vertices. The 242 version offers a sufficient number of parameters to produce detailed-enough models (with 3842 vertices) with respect to the amount of information present in lightcurves. On the other hand, the greater the number of parameters in the modelling, the more computing power, database load and time needed for the inversion process. The number of parameters is therefore a trade-off between models' detail level, computing power needed and time available.

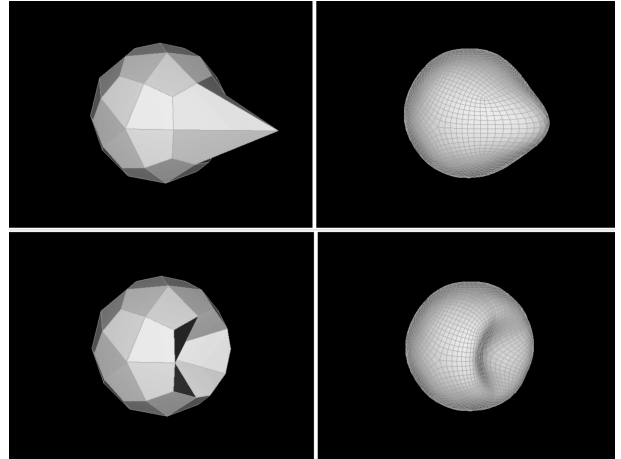


Figure 1. Example of Catmull-Clark algorithm applied to a mesh. Images on the left show initial, rough body, on the right the same body after a surface subdivision. The new mesh is smoother and has more uniformly distributed vertices and faces.

2.2 Orientation in space

Observed photometric lightcurves are compared to models' ones throughout the modelling process. To compute model's lightcurves asteroid's orientation and position in space, as well as the Sun's and the Earth's need to be replicated for the times of the observations. Vectors in the ecliptic reference frame (originating in the Sun's centre) are obtained from NASA JPL's HORIZONS¹ service.

Shape model is defined in its own reference frame, where z axis lies along the model's largest inertia vector (see section 2.3) and constitutes an axis of rotation. The centre of a reference frame is always the centre of mass of a model, assuming even distribution of mass. To orient the model's spin axis Euler angles α , β and γ are used with 3-1-3 rotations about z , x and z axes.

In order to combine translation (orbital position) and spin axis orientation a 4x4 matrix M of a form

$$M = T R_z(\alpha) R_x(\beta) R_z(\gamma) \quad (1)$$

is used, where R stands for a rotation matrix about the axis indicated by the subscript and T stands for translation matrix. Dimensions of M are such that the translation and rotations operations can be represented by a single matrix. Positioning of a model in space, that changes the reference frame from model-centred to the orbital one, is accomplished by multiplying vertices by matrix M .

2.3 Centre of mass and moments of inertia

Every asteroid model created in every sub-step of SAGE method is a physical one, assuming homogeneous density distribution. In order to calculate model's principal axes and define model-centred reference frame the centre of mass needs to be found. Methods described in depth in (Dobrovolskis 1996) are employed for a centre of mass and moments of inertia calculations.

¹ <http://ssd.jpl.nasa.gov/horizons.cgi>

For an arbitrary polyhedron composed of tetrahedrons, a centre of mass vector \mathbf{R} is given by the formula

$$\mathbf{R} = \sum \frac{\Delta V \Delta \mathbf{R}}{V}, \quad (2)$$

where ΔV and $\Delta \mathbf{R}$ are a tetrahedron volume and centroid, V is a polyhedron volume.

Next, an inertia tensor \mathbf{I} of a form

$$\mathbf{I} = \begin{bmatrix} I_{xx} & I_{xy} & I_{xz} \\ I_{xy} & I_{yy} & I_{yz} \\ I_{xz} & I_{yz} & I_{zz} \end{bmatrix}, \quad (3)$$

is calculated. Using parallel axis theorem it is possible to compute an inertia tensor relative to the centre of mass

$$\mathbf{I}' = \mathbf{I} - \mathcal{M} \begin{bmatrix} Y^2 + Z^2 & -XY & -XZ \\ -XY & X^2 + Z^2 & -YZ \\ -XZ & -YZ & X^2 + Y^2 \end{bmatrix}, \quad (4)$$

where \mathcal{M} is total mass of a body and X , Y and Z are Cartesian components of a centre of mass vector \mathbf{R} .

To create body's own reference frame where z axis is the axis of the largest inertia, \mathbf{I}' has to be rotated into new coordinate system in which it becomes diagonal. It is done by finding inertia tensor's eigenvalues.

2.4 Synthetic lightcurve generation

Generating lightcurves of asteroids' models is a computationally expensive process. A shape is described by 3842 vertices on which 7680 faces are defined. SAGE, in general, produces non-convex shapes so shadowing effects have to be taken into account complicating computations even more.

During the modelling process with thousands of iterations, millions of lightcurves are generated; to run SAGE efficiently parallelization of some parts of the calculations is more than necessary. To accelerate the modelling process graphics cards (GPU) and OpenGL² graphics libraries are used. According to our internal tests, the process of rasterization executed on a GPU offers about 100 times speed-up compared to an equivalent code run on a CPU.

To mimic light reflected from a surface, a linear combination of Lambert and Lommel-Seeliger scattering law of a form

$$S = (1 - c) \frac{\mu\mu_0}{\mu + \mu_0} + c\mu\mu_0 \quad (5)$$

is used (Kaasalainen & Torppa 2001), where μ and μ_0 denote cosines of the angles between surface normal and the direction to an observer and direction to the Sun respectively; a linear factor c equals 0.1.

In the process of lightcurve generation a 3D scene is composed in an heliocentric ecliptic reference frame. Camera – an observer – is put in the position of the Earth as it was during the time of the observation. Similarly, asteroid model is translated to its corresponding orbital position and rotations are applied to orient the spin axis of the model. Next, in the process of rasterization an image is created, in

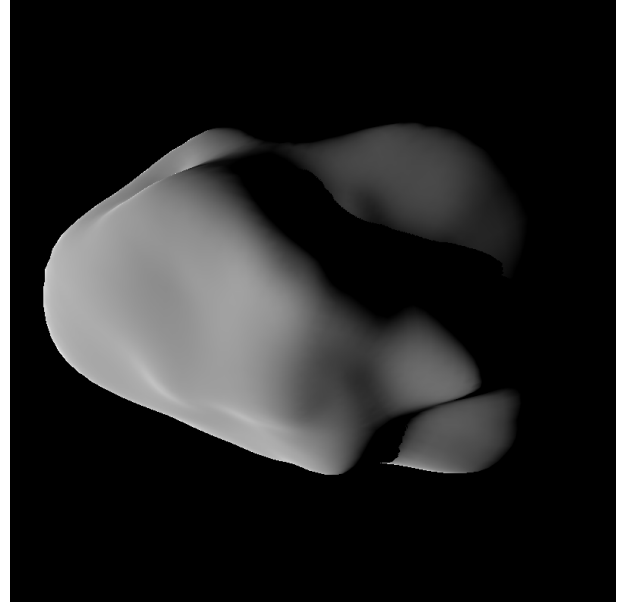


Figure 2. An example of an image generated for lightcurve data point calculation at high phase angle showing self shadowing effect.

which a model is visible as if it was observed from the Earth with a telescope of infinite resolution (Fig. 2). Background has a value of 0 and every surface element has its own colour value computed using the scattering law (Eq. 5). The sum of the pixels' values of an image is one point on a lightcurve. To generate the whole lightcurve, a body is gradually rotated by $\Delta\gamma$ angle and the process ends when a full rotation is performed.

To simulate shadows a scene from the Sun's point of view is generated first. Its goal is to create a shadow map on a model's surface that is used in generating a scene from the Earth's point of view to determine whether a surface element is illuminated or not. This method is fast and produces accurate shadows when only one light source is present.

Generated lightcurves consist of points of relative fluxes. Each point is recalculated to give a magnitude in logarithmic scale so the synthetic lightcurves can be compared with the observed ones. During RMSD calculation a synthetic lightcurve is allowed to shift vertically to find the best fit. It is necessary as most of the time observed lightcurves come from relative photometry, synthetic lightcurve generation does not take into account the distance from an observer to a model, and size and albedo of a body are unknown.

2.5 Period search

During a weighting process, search for best rotational period is performed. The need to repeat the search is justified by changes in shape and pole orientation after every iteration that results in a new set of lightcurves. An example periodogram can be seen in Fig. 3.

The step of the rotation period search is $10^{-6}h$, which is sufficient considering that only small changes to the shape are applied and lightcurves do not change dramatically from one iteration to another.

The whole scope is scanned to search for the period that

² <https://www.opengl.org>

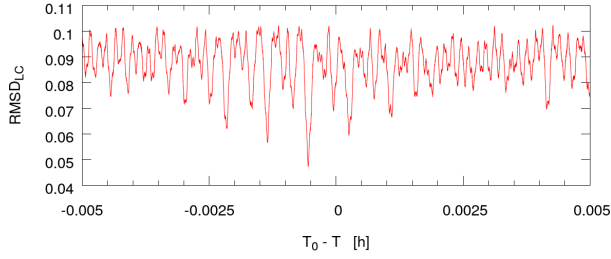


Figure 3. An example periodogram created during search for the best rotational period. Root mean square deviation of all the lightcurves $RMSD_{LC}$ is shown against the difference between initial period T_0 and scanned period T .

results in the best fit for all lightcurves. Observations are performed over many years (at least 3 apparitions needed) and the bigger the time span, the more dramatic the effect of rotation period change, making it easier to find the global minimum. Uncertainty of a period depends on a time range of observations, a period search step and a number of points on synthetic and observed lightcurves. If uncertainty based on observations' time range is smaller than a period search step, the former is used as final period uncertainty.

Synthetic lightcurves are shifted in the time dimension to obtain the best fit determined by overall RMSD value. Each lightcurve comparison is a separate problem, so parallelization can be applied again. CUDA³ libraries are used for a period search to perform necessary computations on GPUs.

Period uncertainty is computed for a final model. It is defined as a range of period values at a σ level calculated as follows:

$$\sigma = \frac{RMSD}{\sqrt{N - n}} \quad (6)$$

where N is a number of points in lightcurves and n is a number of model's degrees of freedom. A value of period uncertainty is different for each model and depends on a data set and model itself.

2.6 Modelling process

A number of free parameters in the modelling process makes brute-force scanning for global minimum impossible. Therefore genetic evolution algorithm is adopted to search for an asteroid model that best fits observations. The modelling process runs on a loop and every iteration generates a new population of random shapes and pole orientations based on the seed shape.

The modelling process does not make any assumptions about shape and pole orientation prior to modelling. A sphere with a random pole orientation is always used as a starting point.

In every iteration a population of shapes is created based on a seed shape by applying small, random changes to parameters describing the shape, so that every model in a population resembles the seed model. The centre of mass and inertia tensor are calculated for every model. Next, a set

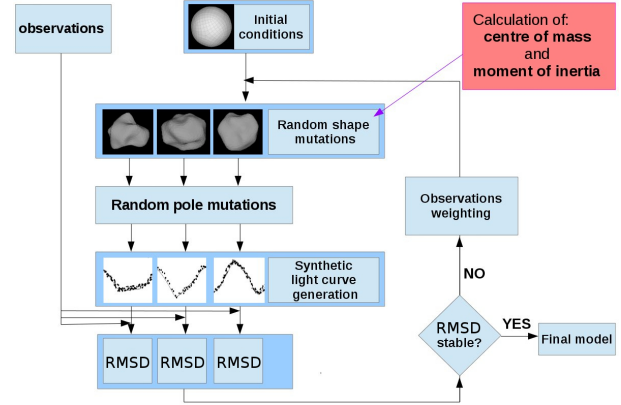


Figure 4. SAGE modelling scheme. See sec 2.6 for description.

of random pole orientations is created to be applied later to the models in a population.

For every combination of shape and pole orientation the synthetic lightcurves are computed (see section 2.4) in order to compare them with the observed ones. To decide which model's lightcurves best resemble the real ones a RMSD (root mean square deviation) value defined as follows

$$RMSD = \sqrt{\frac{1}{n} \sum_i^n (\hat{y}_i - y_i)^2} \quad (7)$$

is used, where n is a number of points on a lightcurve, y_i is an observed magnitude and \hat{y}_i is a computed magnitude. The model with the lowest RMSD value is then chosen as the best one and serves as a seed for the next iteration of the modelling process.

Before a new iteration begins there is an observation weighting step. Every observed lightcurve is compared with a corresponding synthetic one, giving separate RMSD value. Observed lightcurve with the biggest RMSD is given the highest weight directing the flow of models' changes from population to population so that said lightcurve is reproduced better. After a few iterations weights can change and stress is placed on a different lightcurve. This method ensures the modelling process does not fall into a local minimum and is capable of creating a shape that fits all observations.

SAGE algorithm generates models with high accuracy rotation periods, depending on the time span of the observations' set. This is achieved through a rotation period grid search after every iteration during weighting process (see section 2.5).

After choosing the best model in the population its RMSD value is compared with the ones from previous iterations. When RMSD becomes stable (does not change from one iteration to another within a threshold) the modelling process is stopped giving the final model (see top image in Fig. 5).

2.7 Family of solutions

The modelling process described in section 2.6 is run multiple times and every run, starting from a sphere, follows a different path and produces a separate model (Fig. 5).

³ http://www.nvidia.com/object/cuda_home_new.html

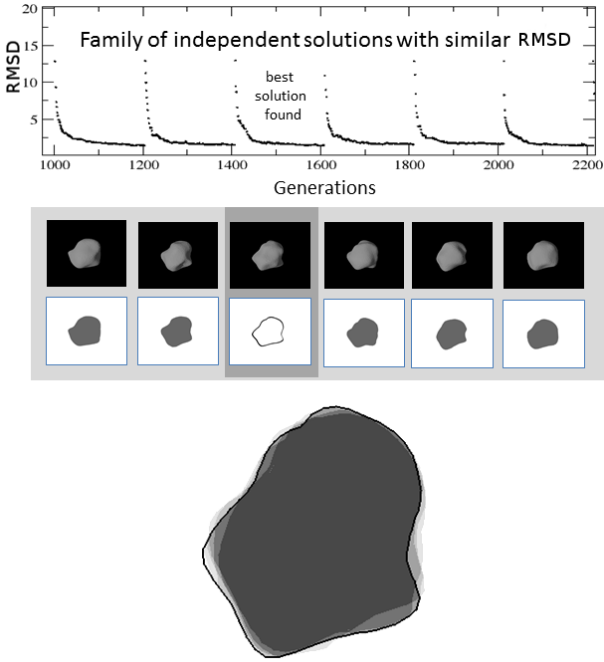


Figure 5. An example of a family of solutions. Top: RMSD shown for multiple runs of modelling process. RMSD value drops fast at the beginning of the modelling gradually plateauing. Middle: different shapes produced by separate modelling runs. Bottom: composition of family of solutions shapes projections on the plane of the sky at an arbitrary epoch, showing the differences between models. The darker the area is the more frequently it appeared in the family. Solid line represents the best shape model found.

This is typical for genetic codes to ensure that the global minimum is found. The collection of models from separate modelling runs is called a family of solutions. In an ideal scenario, when the amount of observational data is sufficient and covers many apparitions of an asteroid (at least 3) all models in a family of solutions are alike.

Most of the time a family of solutions will consist of two subsets of models, one for each possible, ambiguous pole orientation. As mentioned, all models are similar, except models from one subset are flipped by the xy plane with the longitude of the pole λ differing by 180° . These subsets represent the two possible – pro and retrograde – senses of rotation of the same body.

The resulting, final models (one for each of the two pole solutions) are chosen from a family of solutions based on the overall RMSD value describing the fit to all observed lightcurves.

2.8 Convergence

At a first glance, if a small amount of data (e.g. one lightcurve) is given, a genetic algorithm should find a solution quickly. It would be a local minimum – one of many possible shapes able to explain the data. But it is actually not the case. Observational data determine the fitness function (namely, global RMSD) for shapes in randomly generated populations. The smaller the set of data to compare with, the smaller the selective pressure acting on a population. As a result, we deal with genetic drift rather than natural selec-

tion under the fitness function. The algorithm then behaves more like a random walk and actual evolution (changes in models leading to a solution) happens very slowly if it happens at all. It is due to the fact, that parameters' values alterations are rarely reflected in fitness function changes. Therefore, the number of populations, which translates directly into computing time needed, grows dramatically making a genetic algorithm inefficient in such situations.

To minimize the number of iterations and prevent premature convergence from happening, sufficient amount of data is required and it depends on factors such as asteroid's spin axis' orientation, mutual positions of a target and the Earth or data quality, to name a few. This is target specific and cannot be calculated precisely. Before the modelling starts, we can assess the amount of information present in the data by making apparitions' plots (like shown in Fig. 14) to see available geometries or check the coverage and quality of the lightcurves.

2.9 Model validation

The success of modelling depends mainly on a data set. There might be parts of asteroid's surface which are poorly or not at all covered in lightcurves. By studying a family of solutions we can tell if a data set provides good coverage of geometries and grants a unique shape solution. The differences between the models in a family of solutions reveal parts of a shape that were not covered in data, and, if solutions are not alike, modelling is considered inconclusive.

Formally, the best model found has the lowest RMSD value. It is a very good criteria to evaluate a model, but one number does not tell the whole story. What also matters greatly is model's ability to reproduce some distinctive and unique features present in the observed lightcurves without producing additional artifacts. However, some observed features might be bogus making validation process tricky.

During the modelling the best RMSDs found for individual lightcurves are saved. These are the best fits that occurred in the whole process regardless of how they fit other lightcurves. The weighting process is based on these values and disallows a situation where e.g. one lightcurve is perfectly fitted (assuring low overall RMSD) with others fitted poorly. Thanks to that, local minima are avoided and the model explains all the lightcurves at a comparable level.

When dealing with the fact that observed lightcurves are noisy (the noise level being often underestimated or unknown) best RMSDs for individual lightcurves serve as reference points and show what can be achieved based on a given set of observations; this equips us with some additional information about the quality of global RMSD.

3 NUMERICAL TESTS

The setup used in tests represents ideal case for the purpose of testing SAGE's capability of recreating shape, pole orientation and period without any interference that would come from albedo variations, wrong scattering law or uneven mass distribution. The lightcurves are similarly not affected by atmosphere nor by photometric system normally used in asteroid observations.

3.1 Test bodies

To create test models we used Gaussian random sphere generation code based on the algorithm described by Muinonen (1998). The code takes spherical harmonics order and surface grid subdivision depth as input parameters and creates a random body that is later triangulated. Some of the test bodies were further altered by hand to create more extreme cases.

We moved the center of a body to the computed centre of mass and also computed an inertia tensor to align spin axis with the axis of greatest inertia. That simulates homogeneous physical body. We did not introduce any albedo variations on bodies' surfaces.

The shapes and modelling results can be found in appendices available online; the models are labeled with Latin alphabet capital letters. Model A was studied in more detail and is presented below.

3.2 Orbit

We placed test bodies on an artificial circular orbit around a source of light with semimajor-axis $a = 3.5AU$ with orbital period of 6.55 years. Julian day is used to represent time. An observer is situated on a circular, coplanar, non-physical orbit at $1AU$. We created 8 evenly distributed apparitions every 45° (Fig. 6) covering one revolution around the light source. At every apparition lightcurves were created from 5 locations (eq. 8) at the same time, then the whole setup was rotated 45° and $1/8^{th}$ of the orbital period was added to the time. The initial vectors used to place an observer in space were

$$\begin{aligned} \mathbf{v}_1 &= (0, -1, 0)^T \\ \mathbf{v}_2 &= \left(\frac{1}{\sqrt{2}}, -\frac{1}{\sqrt{2}}, 0\right)^T \\ \mathbf{v}_3 &= (1, 0, 0)^T \\ \mathbf{v}_4 &= \left(\frac{1}{\sqrt{2}}, \frac{1}{\sqrt{2}}, 0\right)^T \\ \mathbf{v}_5 &= (0, 1, 0)^T \end{aligned} \quad (8)$$

A test body was put in the position $a\mathbf{v}_3$ in every apparition. As mentioned above, this setup is non-physical (orbital periods of an observer and a test body are the same despite different semimajor-axes) and this experiment could not be replicated in reality. Nonetheless, the relevant aspect is the geometries at which we observe the bodies could be obtained by extending the time of observations, i.e. the lightcurves would not be collected from one revolution but from multiple ones. The actual times of observations are not important. Choosing one particular real-life orbit would produce uneven distribution of apparitions and introduce biases, especially when we reduced the number of apparitions in the tests.

3.3 Lightcurves

Every lightcurve in every apparition covers a full body rotation and consists of 180 evenly distributed points every 2° of the rotation phase.

To create lightcurves for test bodies the same code was used as in SAGE algorithm. This ensures that modeling is

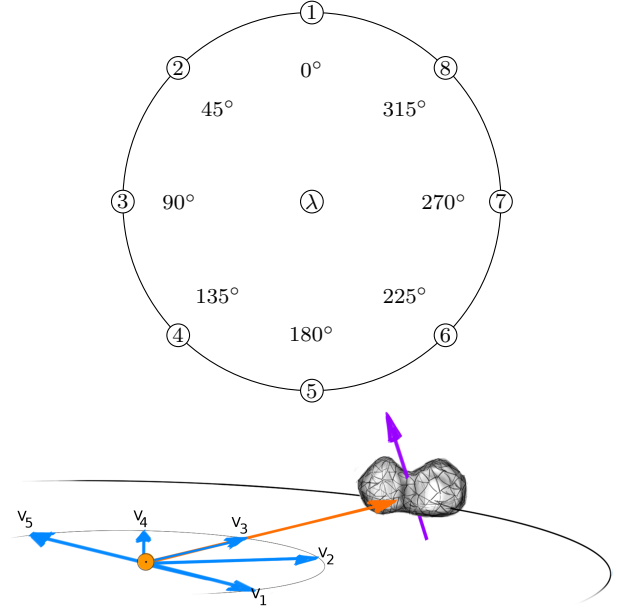


Figure 6. Heliocentric test orbits schema. Top image shows the distribution of apparitions (observer is in the center of the graph). Bottom image represents a setup for single apparition. Vectors v_1 through v_5 define observer's positions while body's position is defined by av_3 . To create 8 different apparitions the initial vectors are rotated about z axis by $45^\circ, 90^\circ, \dots, 315^\circ$.

affected by the same "numerical reality", with exactly the same scattering law, shadowing effects or numerical errors (e.g. floating point rounding). The shape representations however are different, as spherical harmonics were used to create test models and SAGE uses a set of direction fixed vectors. The only similarity lies with models being represented with triangle faces in both cases, but their number and distribution is different as well.

3.4 Modelling

Test bodies were modeled using different sets of data. We varied the amount of apparitions and their distribution on the orbit, the orientation of the spin axis and the phase angle (i.e. the set of observer vectors used in an apparition).

Test body's locations are numbered 1 through 8 and are placed counter-clockwise very 45° (Fig. 6, top graph) starting from $\mathbf{v}_{\text{body}}^{\text{init}} = a(1, 0, 0)^T$. The *app.* abbreviation used in results tables enumerates apparitions' indexes used in the modeling process.

To test the agreement of the models with the test body we constructed topography maps. Given a direction in space we calculated a mean distance from surface elements to the origin within 10° -wide cone and then subtracted the radius of a circumsphere. Each vertex was normalized so the length of most distant vertex from the origin equals 1, therefore the sphere radius is 1 as well.

When we subtract a topography map of a model from a topography map of a test model we get a map of differences between the two. This allows us to compare models and interpret results. A differences map can be displayed directly on the surface of the models in arbitrary orientation.

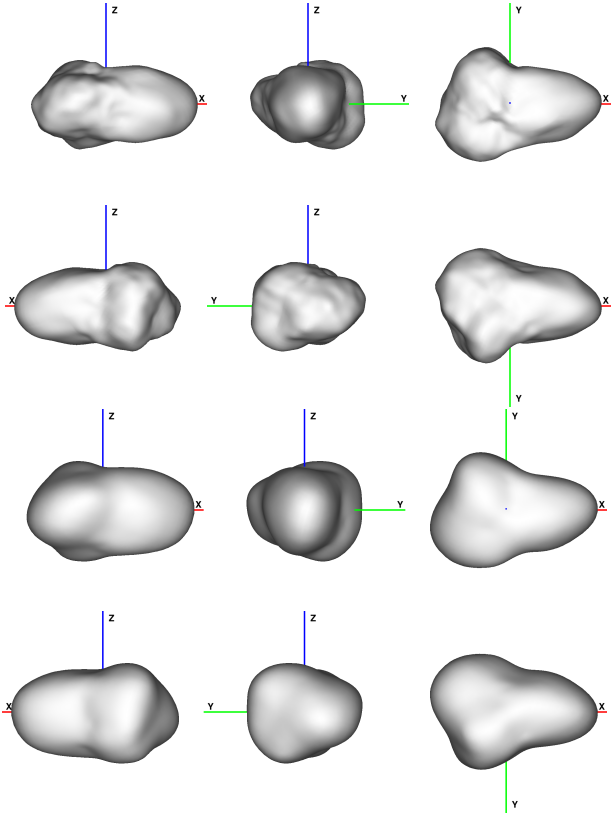


Figure 7. xz , yz , xy , $-xz$, $-yz$ and $-xy$ projections of the test model A. First and second rows: test model, third and fourth rows: the best model A from inversion.

3.5 Results for model A

Table 1 presents a summary of all modelling runs for this model. Model A and its best modelled result can be seen on figure 7 along with topography, pole solution maps and periodogram on figures 8, 9 and 10.

3.5.1 Pole orientation

In each case we received two separate pole solutions with the same β and λ differing by 180° ; shapes for both pole solutions were alike. Table 1 shows the best model found from both sets of pole solutions.

We tested three cases for β : 0° , 45° and 90° . Models with smallest $RMSD_{\text{model}}$ were obtained using all of the apparitions evenly distributed on an orbit and with $\beta = 45^\circ$. In such geometry the whole body is seen by an observer throughout one revolution about a light source, therefore lightcurves may contain information about the whole body. The best fit was $RMSD_{\text{model}} = 0.023411$ for such a case.

For $\beta = 90^\circ$ (i.e an asteroid spin vector pointing north ecliptic pole) lightcurves from all the apparitions consist of the same information as the aspect angle does not change with the position on the orbit therefore the worst fit can be explained. The amount of information is also greatly reduced when $\beta = 0^\circ$ due to the fact that many lightcurves are almost or completely flat.

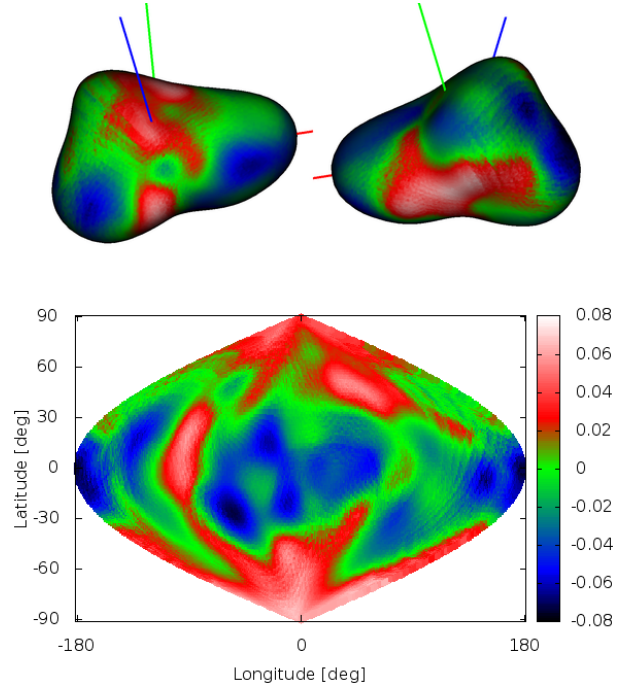


Figure 8. Topography maps for model A. Colours correspond to the difference between test and modelled body in the units of a circumsphere radius. Top row shows the topography map on the surface of the body on two viewing geometries.

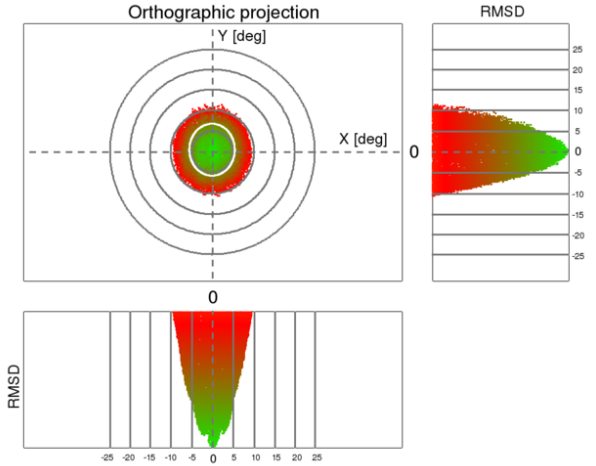


Figure 9. Pole solution map for model A. The map shows coordinates of the best pole solutions projected from the sphere onto a plane. The sphere and plane tangent point is at the position of the test body's correct pole. Colours correspond to RMSD of the solution, green being the best one. The white ellipse represents the variance of the pole solution in the x and y plane coordinates.

3.5.2 Apparitions

Taking into consideration results for eight apparitions with different β we used $\beta = 45^\circ$ for further tests as the best geometry for shape modelling.

As we decreased the number of apparitions and their distribution we obtained worse fits. The 1256 case was the best one among them with $RMSD_{\text{model}} = 0.032389$, con-

Table 1. Tests results summary for models A (Fig. 7), B (Fig. 11), C (Fig. 12) and D (Fig. 13). λ_{init} , β_{init} , λ and β are the test and modelled bodies’ spin axis coordinates respectively, P_{init} and P are rotation periods, *app.* enumerates apparitions used in the modelling (e.g. "1234" means apparitions 1 through 4 were used), θ is a phase angle. $RMSD_{model}$ describes the test and modelled shapes’ fit, while $RMSD_{LC}$ describes test and modelled bodies’ lightcurve fit.

ID	Model	$\lambda_{init} [^\circ]$	$\beta_{init} [^\circ]$	$\lambda [^\circ]$	$\beta [^\circ]$	$P_{init} [h]$	$P [h]$	app.	$\theta [^\circ]$	$RMSD_{model}$	$RMSD_{LC}$
1	A	0	0	–	0 ± 6	12	12.00001 ± 10^{-5}	all 8	0, 14, 16	0.032662	0.006023
2	A	0	90	173 ± 12	90 ± 12	12	12.00001 ± 10^{-5}	all 8	0, 14, 16	0.033616	0.010631
3	A	90	45	89 ± 7	43 ± 7	12	12.00001 ± 10^{-5}	all 8	0, 14, 16	0.023411	0.006601
4	A	90	45	88 ± 8	44 ± 8	12	$11.99999 \pm 4 \cdot 10^{-5}$	1234	0, 14, 16	0.035303	0.008891
5	A	90	45	-90 ± 9	41 ± 9	12	$11.99999 \pm 3 \cdot 10^{-5}$	1256	0, 14, 16	0.032389	0.011149
6	A	90	45	93 ± 9	44 ± 9	12	$11.99997 \pm 3 \cdot 10^{-5}$	1357	0, 14, 16	0.042925	0.010062
7	A	90	45	91 ± 7	44 ± 7	12	12.00001 ± 10^{-5}	all 8	0, 14	0.030033	0.006312
8	A	90	45	90 ± 6	45 ± 6	12	12.00001 ± 10^{-5}	all 8	0	0.037269	0.005038
9	B	290	45	291 ± 13	45 ± 13	6.75	6.75000 ± 10^{-5}	all 8	0, 14, 16	0.026721	0.009015
10	C	330	45	330 ± 7	41 ± 7	12	11.99999 ± 10^{-5}	all 8	0, 14, 16	0.014984	0.005942
11	D	330	45	330 ± 7	41 ± 7	12	11.99999 ± 10^{-5}	all 8	0, 14, 16	0.034730	0.014918

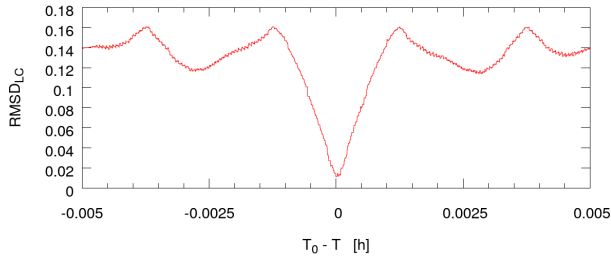


Figure 10. Periodogram for the best result for model A.

sisting of two apparitions 45° apart with additional two corresponding ones on the opposite sides of the orbit. The 1234 case – apparitions from half orbit – was slightly worse ($RMSD_{model} = 0.035303$). The cross-like 1357 apparitions distribution turned out to be significantly worse than the rest with $RMSD_{model} = 0.042925$.

Removing apparitions depletes the amount of information present in the lightcurve dataset making it more difficult for the modelling process to derive shape and pole solutions. Especially in cross-like setup, two of the four apparitions consist of the same information so the effective amount of apparitions is then actually smaller.

3.5.3 Phase angles

The observer’s and model’s positions used when constructing the test model’s lightcurves (fig 6) yield 0° , 14.2° and 15.95° phase angles. We reduced observer’s position vectors to \mathbf{v}_2 , \mathbf{v}_3 and \mathbf{v}_4 giving phase angles 0° and 14.2° in one case

and 0° phase angle exclusively when reduced to \mathbf{v}_3 alone. We used all eight apparitions during the modelling.

The 0° and 14° model had a $RMSD_{model} = 0.030033$; the 0° -only case had $RMSD_{model} = 0.037269$, which is still better than any of the models obtained with smaller number of apparitions. The modelling algorithm was still able to reproduce major concavities although they were rather shallow.

3.6 Other models

We have modelled other test bodies with $\beta = 45^\circ$ to test SAGE’s ability to reconstruct shapes and find pole solutions. The results are summarized in table 1. Models are labeled with capital letters, and their projections can be seen on figures 11, 12 and 13. Diagrams for pole solutions and periods can be seen on figures B1, B2 and B3 in appendices available online.

4 MODELS OF ASTEROIDS

4.1 (433) Eros

Discovered in 1898, Eros is a well studied S-type NEA. Thanks to NEAR Shoemaker orbiter probe and its Laser Rangefinder measurements we have a detailed shape model of this asteroid (Zuber et al. 2000).

With more than one hundred available lightcurves obtained during 5 apparitions (see Tab. 2 for details) Eros is a very good case to test SAGE modelling method. Observations of Eros used for modelling were obtained over large time-span (1951 – 1993), combined with Eros’ orbit

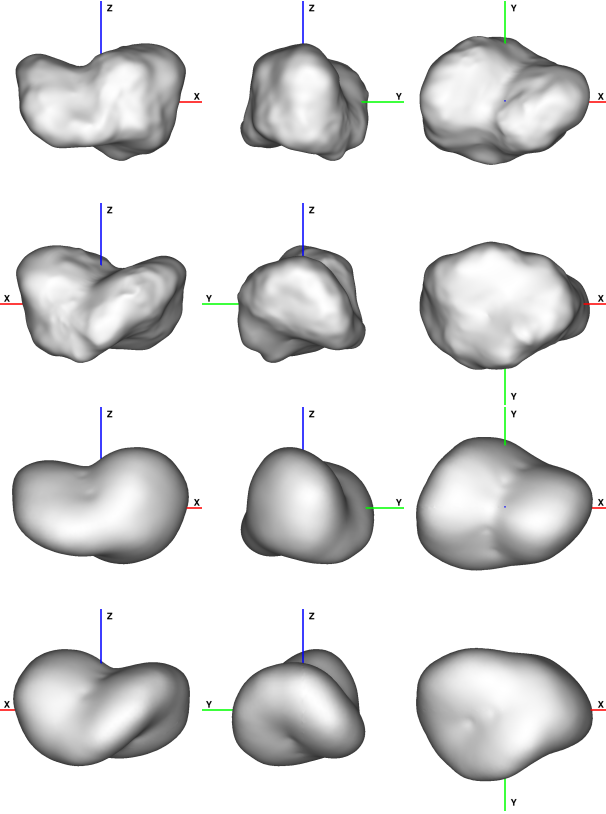


Figure 11. Projections of model B. First and second rows: test model, third and fourth rows: the best model B from inversion.

giving huge span of geometries as seen on Fig. 14. Moreover, some lightcurves were obtained during Eros and the Earth close approaches (1951, 1981, 1974) offering large and varying phase angles.

Eros is a very elongated body which produces lightcurves with amplitudes exceeding 1 magnitude at equatorial aspects. Moreover, Eros has some distinctive surface features, such as a giant crater in the middle, making modelling both interesting and challenging.

Eros model parameters found by SAGE are:

- pole coordinates:

$$\lambda : 17^\circ \pm 5^\circ$$

$$\beta : 8^\circ \pm 5^\circ$$

- rotation period: $5.270256h \pm 10^{-6}h$.

These values are in agreement with the ones found by Miller et al. (2002) based on data from NEAR Shoemaker probe, which was $\lambda = 17.2387^\circ \pm 0.003^\circ$, $\beta = 11.3515^\circ \pm 0.006^\circ$ and $P = 5.27025547h$. The pole solution map can be seen on Fig. 15, while periodogram on Fig. 16.

The presented model of Eros is successfully reproducing lightcurves (see Fig. 17 and Appendix D available online for some examples), and is in very good visual agreement with the high resolution model based on the observations obtained during the NEAR Shoemaker rendezvous (see models' projections in Fig. 18). Having a detailed model from *in situ* measurements allowed us to make a topography map (Fig. 19) as we did in case of test models. The fit was at the level of $\text{RMSD}=0.025959$ with the largest difference of

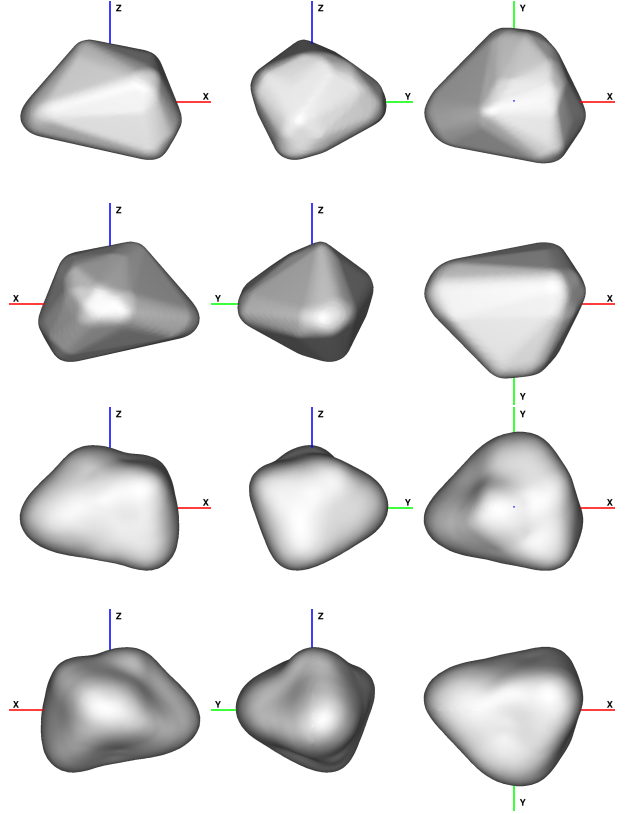


Figure 12. Projections of model C. First and second rows: test model, third and fourth rows: the best model C from inversion.

$0.1R_{max}$. for targets of unknown size we usually scale the shape model so $R_{max} = 1$.

4.2 (9) Metis

Metis, discovered in 1848, is one of the largest main-belt asteroids. The available photometric lightcurve data set is rich and spans over many decades providing good coverage of observing geometries (see Tab. 3 and Fig. 24).

Metis has also been observed using Adaptive Optics and stellar occultation events on several occasions. As Metis has not been visited by any spacecraft to provide *in situ* observations both AO and stellar occultations may serve as the ground truth to validate SAGE model. Moreover stellar occultations allowed us to scale the model.

The preliminary non-convex SAGE model of Metis was first introduced by Bartczak et al. (2014). The model (this work, see Fig. 23 for model's projections and Fig. 20 for periodogram) successfully reproduces photometric observations of Metis (see Fig. 22). Fig. E1 shows the lightcurve comparison with other published models of Metis by: Hanuš et al. (2013), Torppa et al. (2003) and Viikinkoski et al. (2015).

SAGE model parameters:

- pole coordinates:

$$\lambda : 182^\circ \pm 4^\circ$$

$$\beta : 20^\circ \pm 4^\circ$$

- rotation period: $5.079177h \pm 10^{-6}h$.
- R_{max} : 110km

Table 2. Details of the lightcurve data used for 433 Eros modelling. α – phase angle, λ – ecliptic longitude, β – ecliptic latitude.

Apparition	Year	N_{lc}	α [°]	λ [°]	β [°]	reference
1	1951/1952	28	18.6 – 59.2	5.1 – 118.5	-10.3 – 21.5	Beyer (1953),
2	1972	1	17.2	341.5	8.5	Dunlap (1976)
3	1974/1975	68	8.6 – 44.3	52.5 – 158.0	-31.0 – 33.8	Cristescu (1976), Dunlap (1976), Millis et al. (1976), Miner & Young (1976), Pop & Chis (1976), Scaltriti & Zappala (1976), Tedesco (1976)
4	1981/1982	4	28.6 – 53.5	42.4 – 125.6	-18.6 – 36.7	Drummond et al. (1985), Harris et al. (1999)
5	1993	8	1.0 – 18.1	296.1 – 308.3	-0.8 – 3.9	Krugly & Shevchenko (1999)

Table 3. Details of the lightcurve data used for 9 Metis modelling. α – phase angle, λ – ecliptic longitude, β – ecliptic latitude.

Apparition	Year	N_{lc}	α [°]	λ [°]	β [°]	reference
1	1949	1	2.5	41.1	-5.0	Groeneveld & Kuiper (1954a)
2	1954	4	3.0 – 9.4	97.4	5.6	Groeneveld & Kuiper (1954b)
3	1958	1	5.1	153.1	9.6	Gehrels & Owings (1962)
4	1962	2	3.5–5.1	195.0	7.8	Chang & Chang (1962)
5	1964	1	16.4	94.5	1.5	Yang et al. (1965)
6	1974	1	8.5	294.0	-5.3	Zappala & van Houten-Groeneveld (1979)
7	1978	3	4.3 – 13.2	320.0	-9.0	Schober & Surdej (1979)
8	1979	3	23.0 – 24.2	140.2	6.0	Harris & Young (1989)
9	1982/1983	3	8.5 – 24.0	32.0	-1.1	di Martino & Cacciatori (1984), Weidenschilling et al. (1987)
10	1984	8	3.5 – 13.5	178.0	8.9	Zeigler & Florence (1985), di Martino et al. (1987), Weidenschilling et al. (1987)
11	1985	2	4.4 – 5.2	286.0	-4.8	Weidenschilling et al. (1987)
12	1986	3	2.2 – 3.8	67.0	-0.8	Melillo (1987)
13	1988	2	2.3 – 2.8	214.0	5.0	Weidenschilling et al. (1990)

4.2.1 Stellar occultations

Metis had multiple stellar occultations events, but only 2008 and 2014 events were usable for shape fitting. These direct shape measurements can be used for both model validation and scaling. We matched our Metis model silhouettes against occultations’ chords and compared with Metis models obtained using KOALA (Hanus̄ et al. 2013) (using lightcurves and adaptive optics) and ADAM (Hanus̄ et al. 2017) (using lightcurves, adaptive optics and stellar occultations) methods and the convex model by Torppa et al. (2003).

To find the best fit we created the model’s silhouette for a given date and matched it against chords produced by stellar occultations’ timings. The silhouette was moved in x and y axes (i.e. on Earth’s surface) and scaled to provide the best fit. Figure 25 shows the best fit of Metis models from various techniques.

Tab. 4 shows equivalent volume sphere diameters and densities from publications on available Metis models. Volumes and maximal radii (and density in case of convex model) were computed for the purpose of this work from 3D shape models for further comparison. To be able to compare models scaled with stellar occultations we used our software on all of the models. Diameters, volumes and densities calculated from 2008 and 2014 stellar occultation events shown in Tab. 5 are in agreement with the ones in Tab. 4 which proves robustness of our occultation fitting software.

We treated occultation chords from 2008 and 2014 separately to see if the models explain both sets of observations equally well. Vertex meshes were used to find volumes and subsequently calculate equivalent sphere diameters. Densities were determined using Metis’ mass from Carry (2012) with density uncertainty $\delta\rho$ given by

$$\delta\rho = \rho\sqrt{\left(\frac{\delta M}{M}\right)^2 + \left(\frac{\delta V}{V}\right)^2} \quad (9)$$

where M and V are mass and volume, whereas δM and δV are mass and volume uncertainties. Scalings of SAGE Metis model from separate occultation events are consistent and in agreement with values derived for other Metis models.

4.2.2 Adaptive Optics

We have combined the AO images from Hanus̄ et al. (2017) with Metis models’ sky projections for observation dates (Fig. 26). Visual inspection indicates SAGE model matches AO observations. There is also a strong resemblance between SAGE and ADAM models.

5 CONCLUSIONS

We have developed a new modelling method – called SAGE – based on photometric lightcurves, reconstructing non-convex shapes, spin axis orientations and rotation periods

Table 4. The length of the longest vector R_{max} , equivalent volume sphere diameter D , volume V and density ρ of (9) Metis published models from different modelling methods. The mass $M = 8.39 \pm 1.67[10^{18}kg]$ for density calculation was taken from Carry (2012).

model	R_{max} [km]	D [km]	V [$10^6 km^3$]	ρ [gcm^{-3}]
CONVEX	114.5	169 ± 20 (Durech et al. 2011)	2.52 ± 0.89	3.33 ± 1.35
KOALA	102.0	153 ± 11 (Hanus et al. 2013)	1.87 ± 0.40	4.47 ± 1.07 (Hanus et al. 2013)
ADAM	111.6	168 ± 3 (Hanus et al. 2017)	2.46 ± 0.13	3.4 ± 0.7 (Hanus et al. 2017)

Table 5. (9) Metis models sizes R_{max} , equivalent volume sphere diameter D , volume V and density ρ calculated based on 2008 and 2014 stellar occultations. Mass $M = 8.39 \pm 1.67[10^{18}kg]$ (Carry 2012).

model	2008				2014			
	R_{max} [km]	D [km]	V [$10^6 km^3$]	ρ [gcm^{-3}]	R_{max} [km]	D [km]	V [km^3]	ρ [gcm^{-3}]
CONVEX	115 ± 5	170 ± 7	2.56 ± 0.33	3.27 ± 0.77	112 ± 5	165 ± 7	2.36 ± 0.31	3.54 ± 0.85
KOALA	112 ± 4	168 ± 6	2.48 ± 0.26	3.38 ± 0.76	115 ± 7	172 ± 10	2.68 ± 0.49	3.12 ± 0.84
ADAM	110 ± 3	165 ± 4	2.36 ± 0.19	3.55 ± 0.76	112 ± 4	168 ± 6	2.49 ± 0.26	3.36 ± 0.76
SAGE	106 ± 3	165 ± 5	2.36 ± 0.20	3.54 ± 0.76	107 ± 5	167 ± 8	2.43 ± 0.34	3.44 ± 0.84

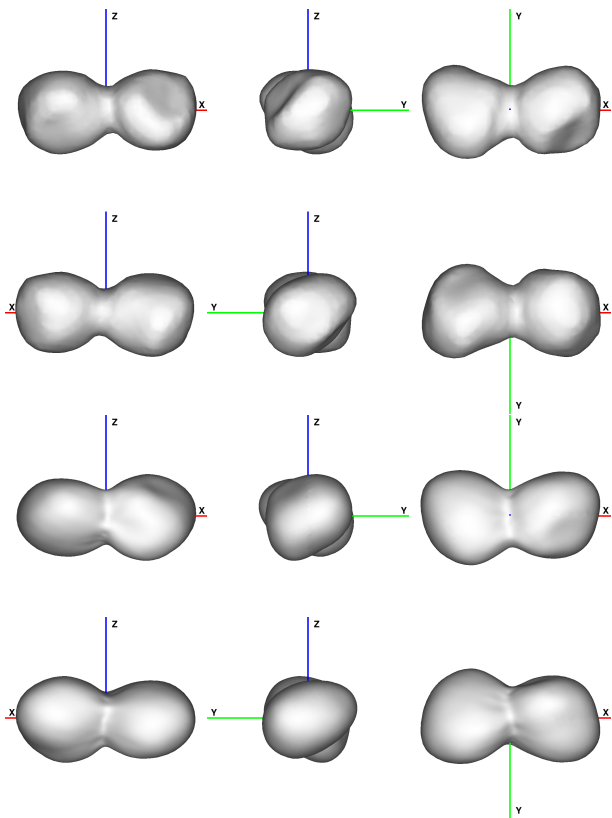


Figure 13. Projections of model D. First and second rows: test model, third and fourth rows: the best model D from inversion.

of asteroids. The method is based on a genetic algorithm that converges to a stable solution over many iterations of random shape and spin axis mutations.

Being computationally expensive, SAGE is run on a computer cluster of multiple nodes equipped with graphics cards that are performing calculations when parallelization

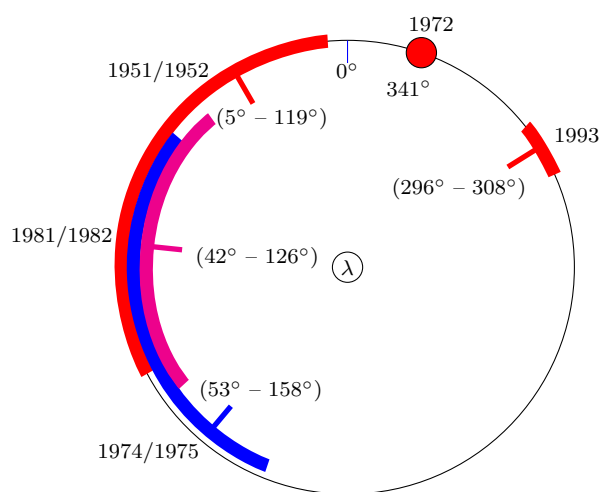


Figure 14. The distribution of Eros apparitions. λ denotes J2000 ecliptic longitude of the asteroid.

is possible, e.g. models' lightcurve computation or search for a rotational period.

To evaluate method's capabilities we have performed numerical tests during which SAGE attempted to deliver a model that best fit given lightcurves. SAGE recreated test models accurately when provided with favorable geometries: the $\beta = 45^\circ$ and evenly distributed apparitions with $0^\circ - 16^\circ$ phase angles producing non-flat lightcurves containing information about the whole body. In other cases, as tests on model A indicated, the differences between a model and a resulting model increased; the worst fit was with 0° -phase-angle-only data. The general shape was recreated, but concavities on the shape were shallow. In each case the biggest difference between test and modelled shapes was around the south and north poles due to z -axis scale uncertainty. We have tested different kinds of shapes, from random gaussian shapes to contact binary-like body. SAGE's shape representation (fixed vectors) was fit to describe each of them.

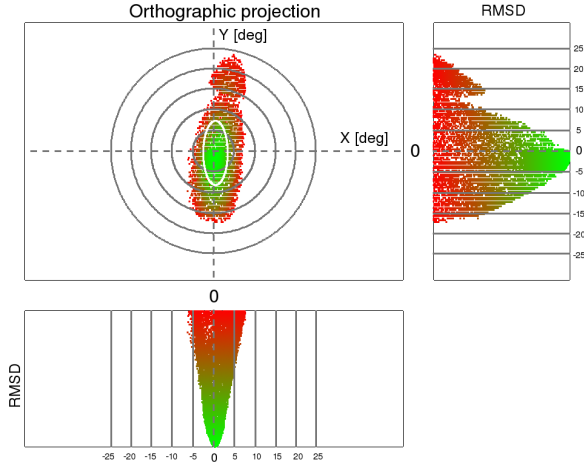


Figure 15. Pole solution map for (433) Eros model.

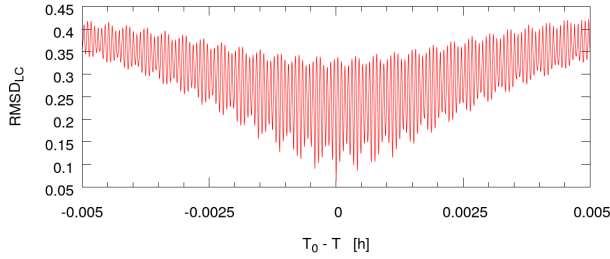


Figure 16. Periodogram for (433) Eros.

We picked (433) Eros and (9) Metis asteroids to test SAGE on real observational data. Our choice was determined by the availability of the data (detailed shape model from NEAR Shoemaker probe for Eros and stellar occultations and adaptive optics observations for Metis) that we were able to compare to, as well as plethora of photometric data.

The (433) Eros model reproduces general shape and major features of the asteroid (Fig. 18). The maximum deviation from NEAR shape (Fig. 19) is in order of 0.1 of the R_{max} with total $RMSD=0.025959$. The rotation axis orientation $\lambda = 17^\circ \pm 5^\circ$, $\beta = 8^\circ \pm 5^\circ$ and period $P = 5.270256h \pm 10^{-6}h$ are in agreement with the values found by Miller et al. (2002).

The (9) Metis model reproduces lightcurves very well. The pole solution found by SAGE is $\lambda = 182^\circ \pm 4^\circ$, $\beta = 20^\circ \pm 4^\circ$ with the rotation period $P = 5.079177h \pm 10^{-6}h$. By comparing the model with 2008 and 2014 stellar occultations we scaled it and obtained $R_{max}^{2008} = 106 \pm 3km$, $R_{max}^{2014} = 107 \pm 5km$ which yield equivalent volume sphere diameter of $D^{2008} = 165 \pm 5km$, $D^{2014} = 167 \pm 8km$; assuming the mass $M = 8.39 \pm 1.67 \cdot 10^{18}kg$ the density is $\rho^{2008} = 3.54 \pm 0.76 \frac{g}{cm^3}$, $\rho^{2014} = 3.44 \pm 0.84 \frac{g}{cm^3}$. As seen in Tab. 5 these values do not deviate significantly from the ones calculated for ADAM model, which was based on lightcurves, stellar occultations and adaptive optics. A comparison with adaptive optics observations (Fig. 26) also validates SAGE model.

Tests and asteroids' models described in this work demonstrate SAGE's ability to model asteroids' physical pa-

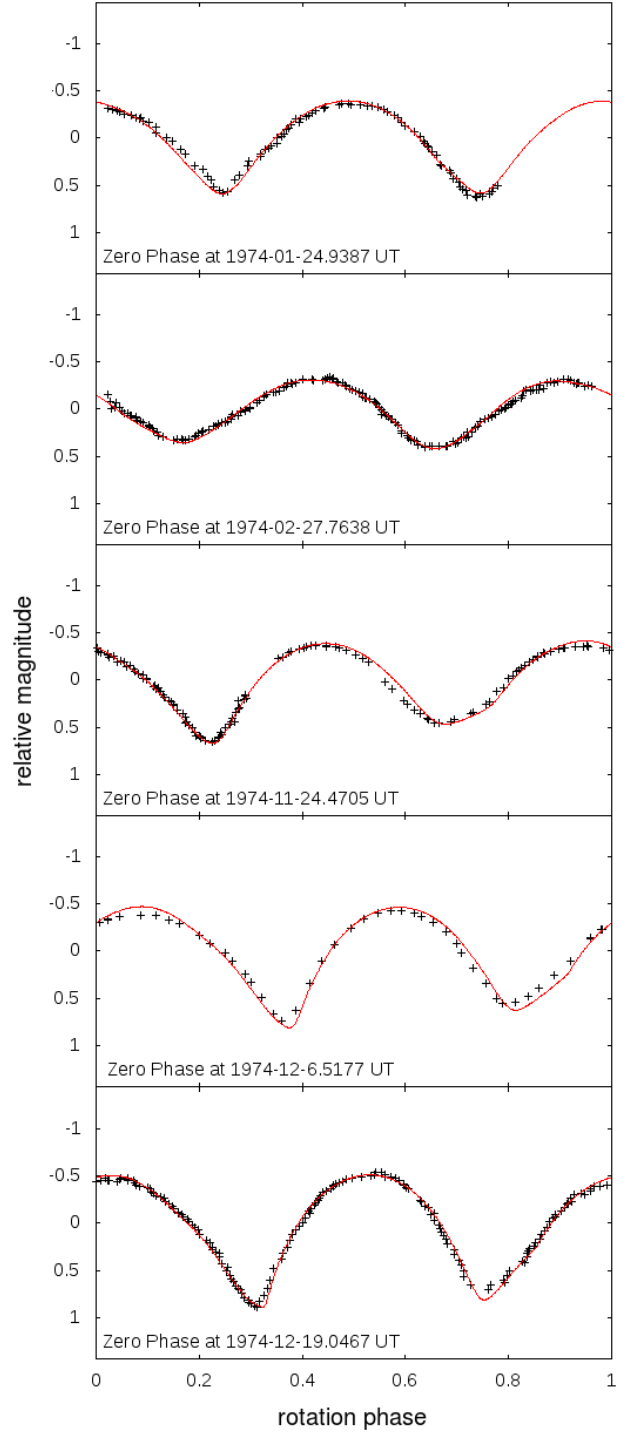


Figure 17. Eros model fit (solid line) to some of the photometric lightcurves (dots). The data from top to bottom: Beyer 1953, Dunlap 1976, Cristescu 1976, Durmmond et al. 1985, Krugly & Shevchenko 1999.

rameters and create their non-convex shapes without making any prior assumptions, except for uniform albedo, homogeneous mass distribution and principal axis rotation. SAGE's software design allows to extend the algorithm to include other types of asteroid observation techniques, e.g. stellar occultations and adaptive optics. A merge with radar delay-Doppler observations was already tested in Dudziński

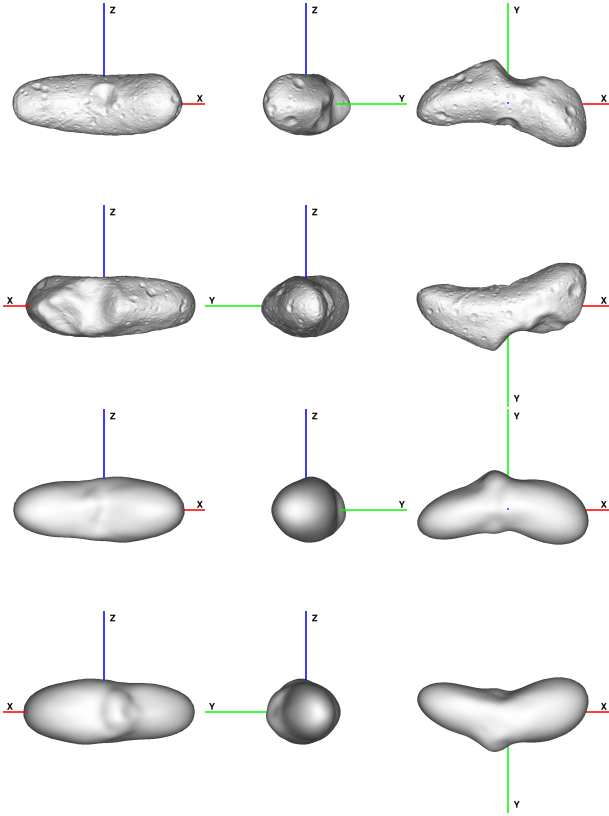


Figure 18. Projections of (433) Eros model obtained from NEAR Shoemaker mission (first and second rows), and SAGE model of Eros from photometry (third and fourth rows).

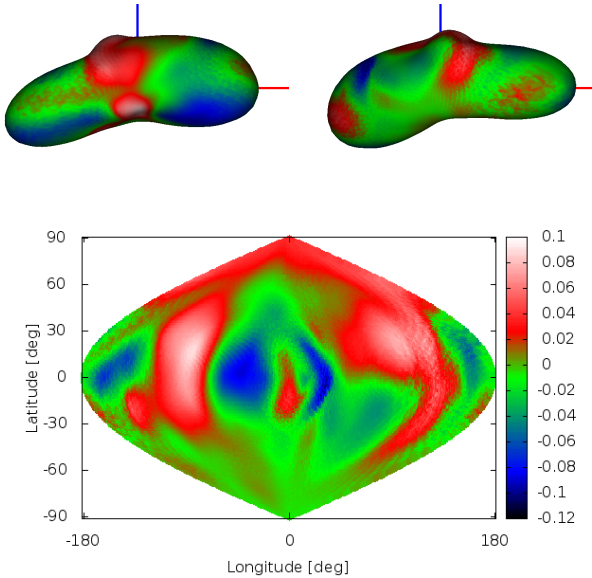


Figure 19. Topography map for (433) Eros SAGE model by comparison with Eros' model form NEAR.

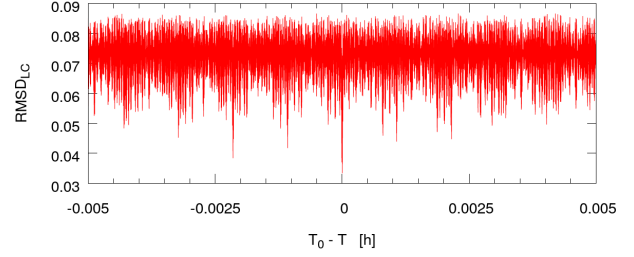


Figure 20. Periodogram for (9) Metis.

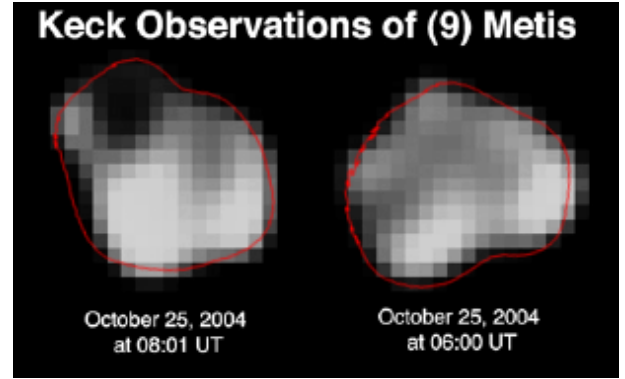


Figure 21. Profile comparison of the best solution found for the (9) Metis non-convex shape model (this work) to the Adaptive Optics observations presented in Marchis et al. (2006) obtained with the Keck NGS AO system.

& Bartczak (2016). This additional data will definitely help place more constraints during the modelling process and produce models of better quality.

ACKNOWLEDGEMENTS

The research leading to these results has received funding from the European Union's Horizon 2020 Research and Innovation Programme, under Grant Agreement no 687378.

This work was partially supported by grant no. 2014/13/D/ST9/01818 from the National Science Centre, Poland.

REFERENCES

- Bartczak P., Santana-Ros T., Michalowski T., 2014, in Muinonen K., Penttilä A., Granvik M., Virkki A., Fedorets G., Wilkman O., Kohout T., eds, *Asteroids, Comets, Meteors 2014*.
 Beyer M., 1953
 Carry B., 2012, *Planet. Space Sci.*, 73, 98
 Carry B., et al., 2010, *Icarus*, 205, 460
 Carry B., et al., 2012, *Planet. Space Sci.*, 66, 200
 Catmull E., Clark J., 1978, *Computer-Aided Design*, 10, 350
 Cellino A., Zappala V., di Martino M., 1987, *Publications of the Astronomical Institute of the Czechoslovak Academy of Sciences*, 67, 121
 Chang Y. C., Chang C. S., 1962, *Acta Astron. Sinica*, 10, 101
 Cristescu C., 1976, *Icarus*, 28, 39
 Dobrovolskis A. R., 1996, *Icarus*, 124, 698
 Drummond J. D., Cocke W. J., Hege E. K., Strittmatter P. A., 1985, *Icarus*, 61, 132

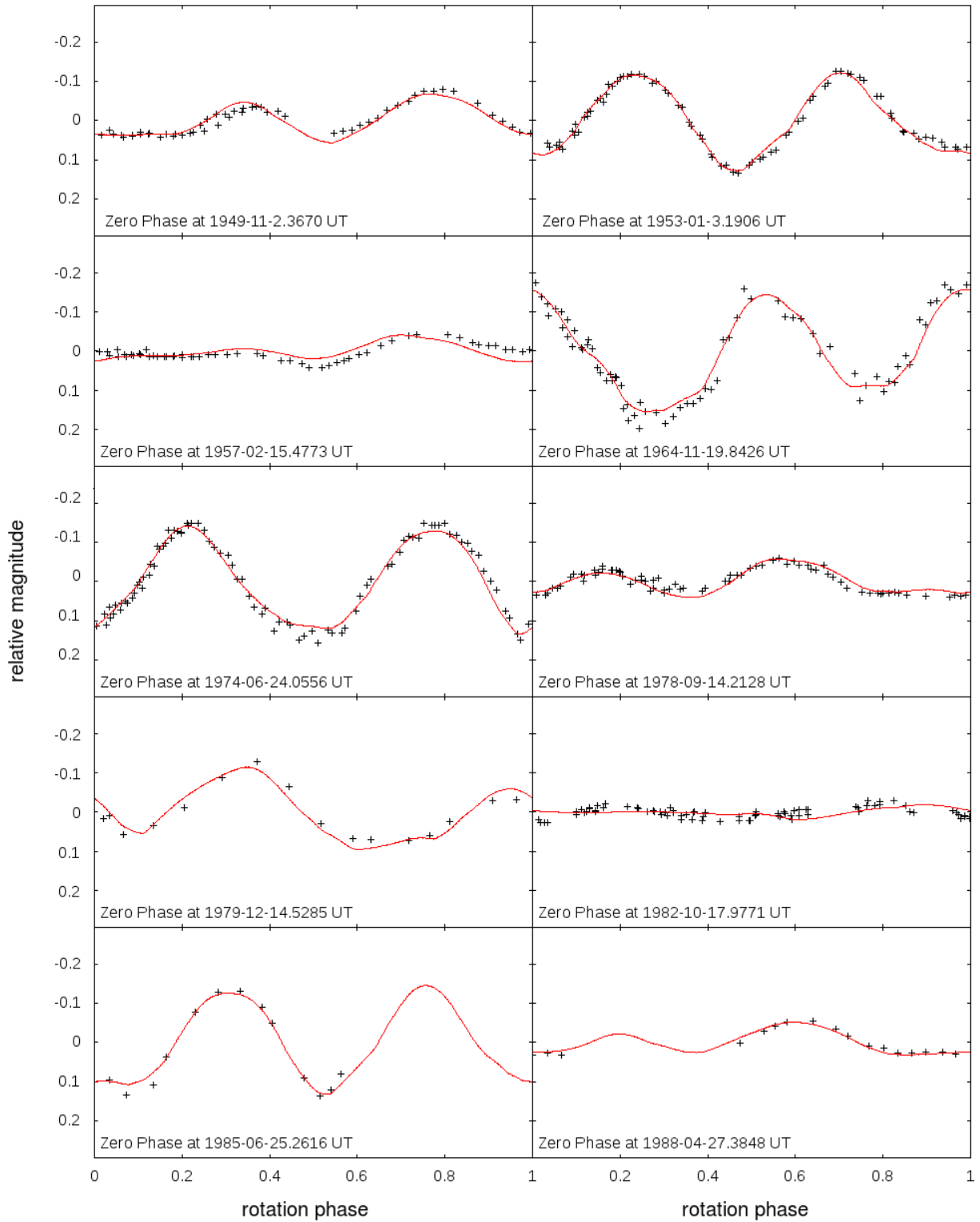


Figure 22. Metis filter fit to some observations. The solid line is the synthetic brightness associated with the model solution, while the dots correspond to the photometric observations. Please notice that a different magnitude scale has been used for each observation for clarity purposes.

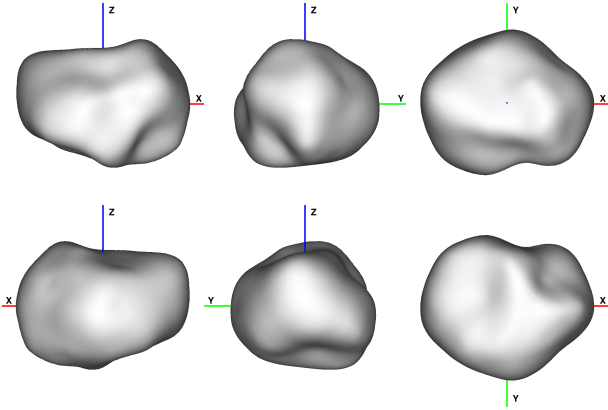


Figure 23. Projections of (9) Metis asteroid model from SAGE.

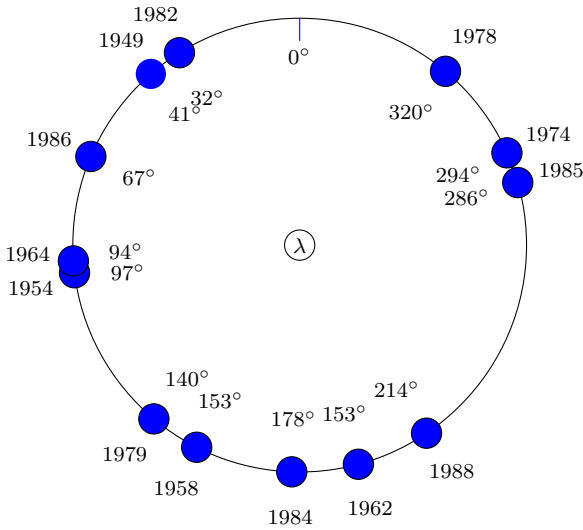


Figure 24. Distribution of apparitions for Metis.

- Marchis F., Kaasalainen M., Hom E. F. Y., Berthier J., Enriquez J., Hestroffer D., Le Mignant D., de Pater I., 2006, *Icarus*, **185**, 39
- Melillo F. J., 1987, *Minor Planet Bulletin*, **14**, 21
- Michalowski T., 1993, *Icarus*, **106**, 563
- Miller J. K., et al., 2002, *Icarus*, **155**, 3
- Millis R. L., Bowell E., Thompson D. T., 1976, *Icarus*, **28**, 53
- Miner E., Young J., 1976, *Icarus*, **28**, 43
- Muinenen K., 1998, *A&A*, **332**, 1087
- Pop V., Chis D., 1976, *Icarus*, **28**, 37
- Russell H. N., 1906, *Astrophysical Journal*, **24**, 1
- Scaltriti F., Zappala V., 1976, *Icarus*, **28**, 29
- Schober H. J., Surdej J., 1979, *A&AS*, **38**, 269
- Tedesco E. F., 1976, *Icarus*, **28**, 21
- Torppa J., Kaasalainen M., Michalowski T., Kwiatkowski T., Kryszczyńska A., Denchev P., Kowalski R., 2003, *Icarus*, **164**, 346
- Uchida K., Goguen J. D., 1987, *Bulletin of the American Astronomical Society*, **19**, 842
- Viikinkoski M., Kaasalainen M., Durech J., 2015, *A&A*, **576**, A8
- Weidenschilling S. J., Chapman C. R., Davis D. R., Greenberg R., Levy D. H., Vail S., 1987, *Icarus*, **70**, 191
- Weidenschilling S. J., Chapman C. R., Davis D. R., Greenberg R., Levy D. H., 1990, *Icarus*, **86**, 402
- Yang X. Y., Zhang Y. Y., Li X. Q., 1965, *Acta Astron. Sinica*, **13**, 66
- Zappala V., van Houten-Groeneveld I., 1979, *Icarus*, **40**, 289
- Zeigler K. W., Florence W. B., 1985, *Icarus*, **62**, 512
- Zuber M. T., et al., 2000, *Science*, **289**, 2097
- di Martino M., Cacciatori S., 1984, *Icarus*, **60**, 75
- di Martino M., Zappala V., de Sanctis G., Cacciatori S., 1987, *Icarus*, **69**, 338

- Dudzinski G., Bartczak P., 2016, in *AAS/Division for Planetary Sciences Meeting Abstracts*. p. 326.06
- Dunlap J. L., 1976, *Icarus*, **28**, 69
- Đurech J., et al., 2011, *Icarus*, **214**, 652
- Gehrels T., Owings D., 1962, *ApJ*, **135**, 906
- Groeneveld I., Kuiper G. P., 1954a, *ApJ*, **120**, 200
- Groeneveld I., Kuiper G. P., 1954b, *ApJ*, **120**, 529
- Hanuš J., Marchis F., Đurech J., 2013, *Icarus*, **226**, 1045
- Hanuš J., et al., 2017, preprint
- Harris A. W., Young J. W., 1989, *Icarus*, **81**, 314
- Harris A. W., Young J. W., Bowell E., Tholen D. J., 1999, *Icarus*, **142**
- Kaasalainen M., Torppa J., 2001, *Icarus*, **153**, 24
- Kaasalainen M., Torppa J., Muinenen K., 2001, *Icarus*, **153**, 37
- Kaasalainen M., Viikinkoski M., Carry B., Durech J., Lamy P., Jorda L., Marchis F., Hestroffer D., 2011, in *EPSC-DPS Joint Meeting 2011*. p. 416
- Karttunen H., Bowell E., 1989, *Astronomy and Astrophysics*, **208**, 320
- Krugly Y. N., Shevchenko V. G., 1999, in *Lunar and Planetary Science Conference*.
- Magnusson P., Barucci M. A., Drummond J. D., Lumme K., Ostro S. J., Surdej J., Taylor R. C., Zappala V., 1989, in *Binzel R. P., Gehrels T., Matthews M. S., eds., Asteroids II*. University of Arizona Press, pp 66–97

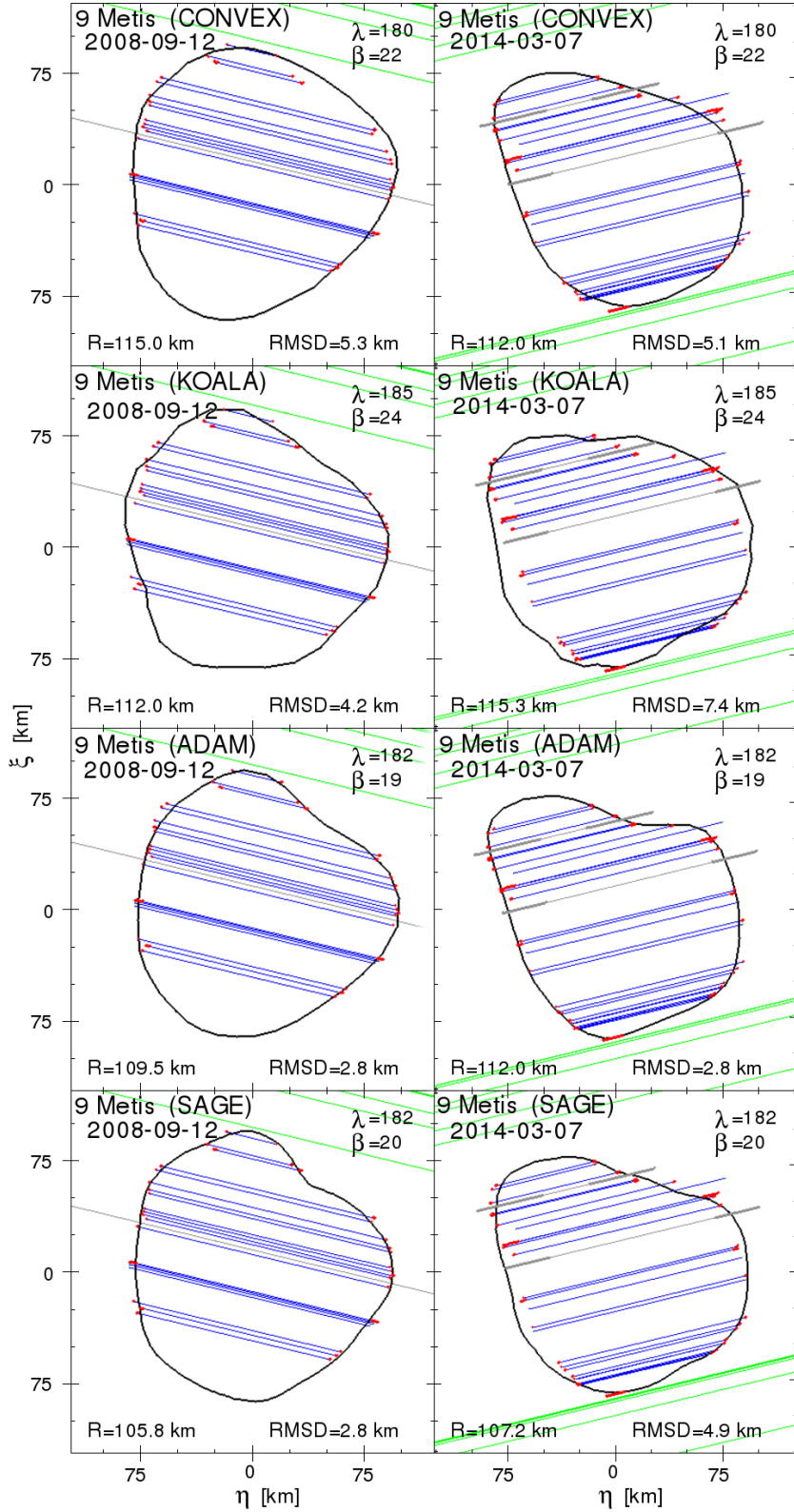


Figure 25. Metis models' silhouettes matched with 2008 and 2014 stellar occultations. χ^2 value is calculated by summing the distances from the ends of the chords to the point on the silhouette along the chord direction. The R value is the size of the model, i.e. the length of the longest vector in the model, based on the fit. The red colour at the end of the chords mark the error of the position based on the timing uncertainty. From the top: convex model (Torppa et al. 2003), KOALA (Hanuš et al. 2013), ADAM (Viikinkoski et al. 2015), SAGE (this work).

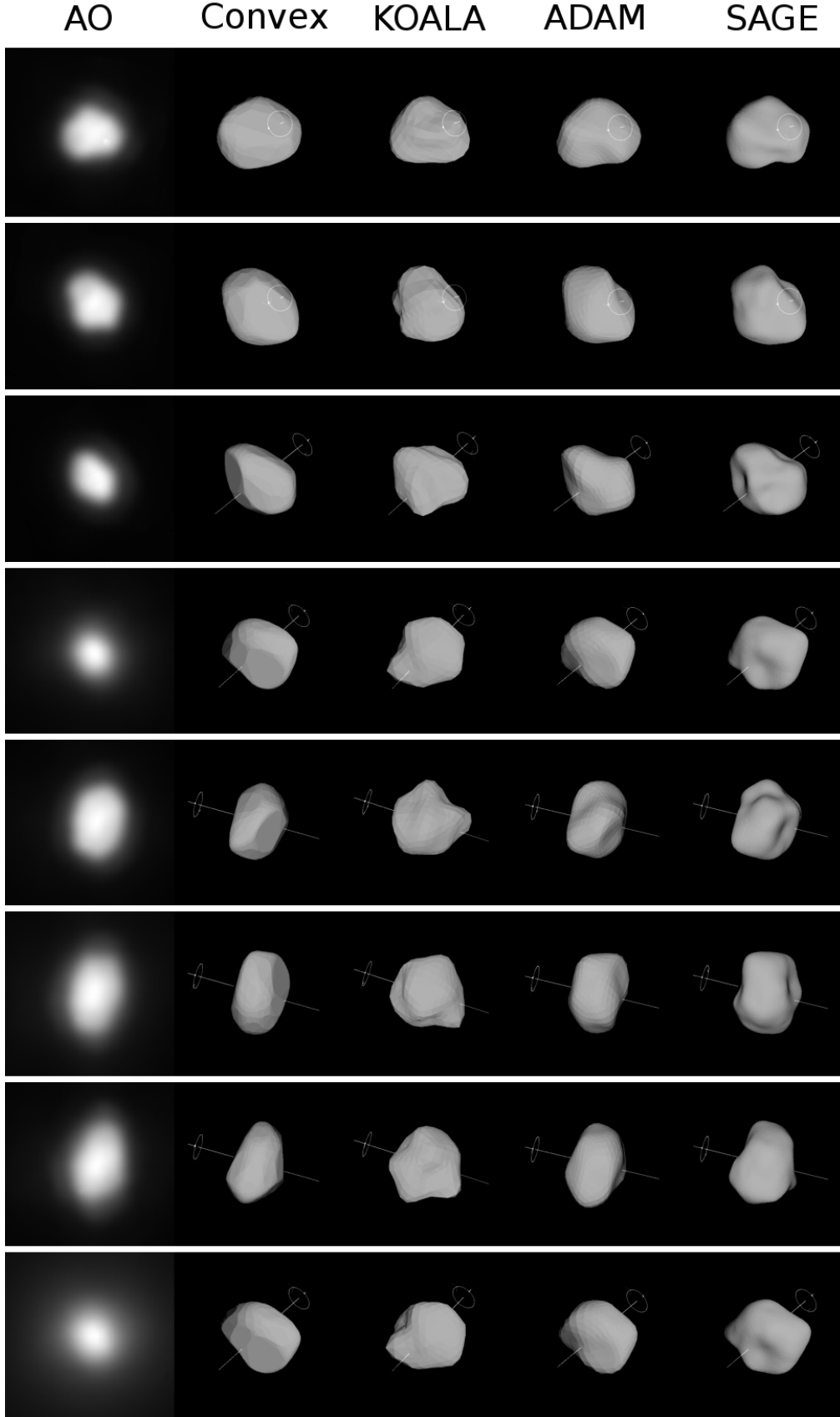


Figure 26. Comparison between various Metis models (Convex (Torppa et al. 2003), KOALA (Hanus et al. 2013), ADAM (Viikinkoski et al. 2015), SAGE—this work) and Adaptive Optics observations (Hanus et al. 2017). From the top, the dates and UT times of the observations are: 2004-10-25 05:57:31; 2004-10-25 07:57:22; 2003-06-05 10:57:09; 2003-07-14 06:29:07; 2012-12-29 12:09:55; 2012-12-29 13:34:42; 2012-12-29 14:24:52; 2003-07-14 06:42:46.

APPENDIX A: TOPOGRAPHY AND POLE SOLUTION MAPS WITH PERIODOGRAMS FOR MODEL A

APPENDIX B: RESULTS FOR MODELS B, C AND D

APPENDIX C: TEST MODELS' LIGHTCURVES

APPENDIX D: (433) EROS LIGHTCURVES

Some of the Eros lightcurves compared with model's ones.

APPENDIX E: (9) METIS LIGHTCURVES

Comparison of lightcurves of available Metis models from various methods.

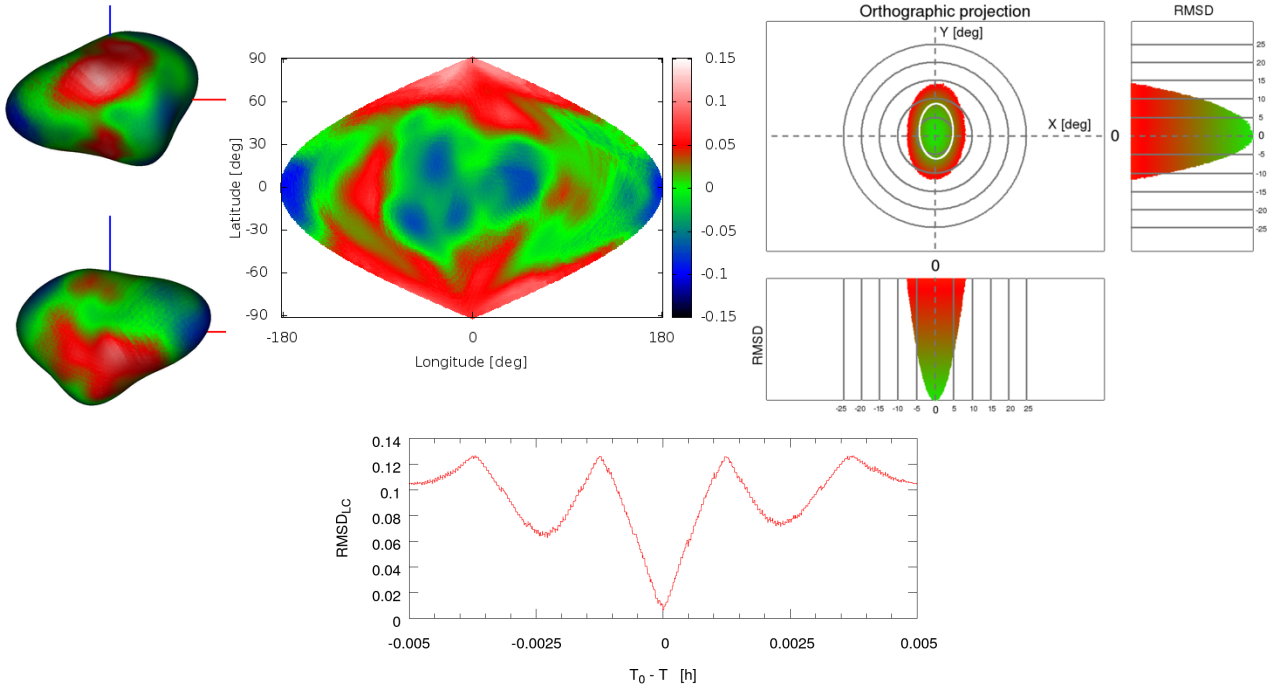


Figure A1. Topography and pole solution maps with periodogram for model A, $\beta = 0^\circ$, phase angles 0° , 14° , 16° , all apparitions.

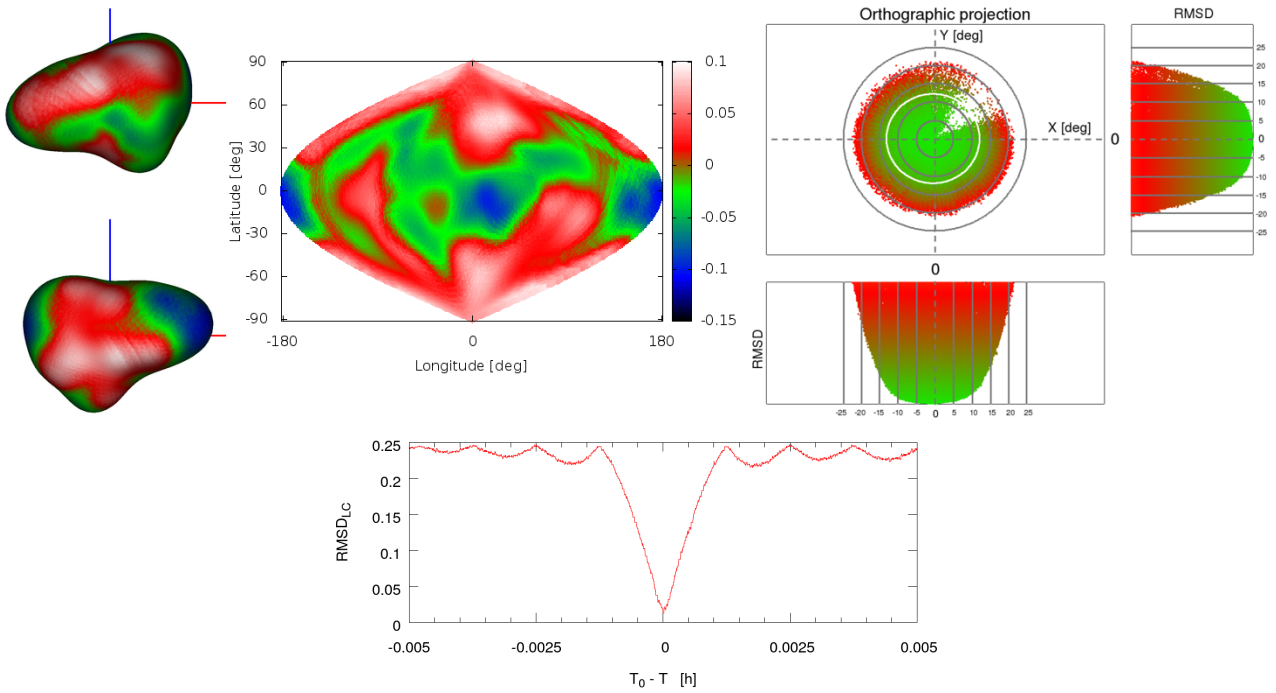


Figure A2. Topography and pole solution maps with periodogram for model A, $\beta = 90^\circ$, phase angles 0° , 14° , 16° , all apparitions.

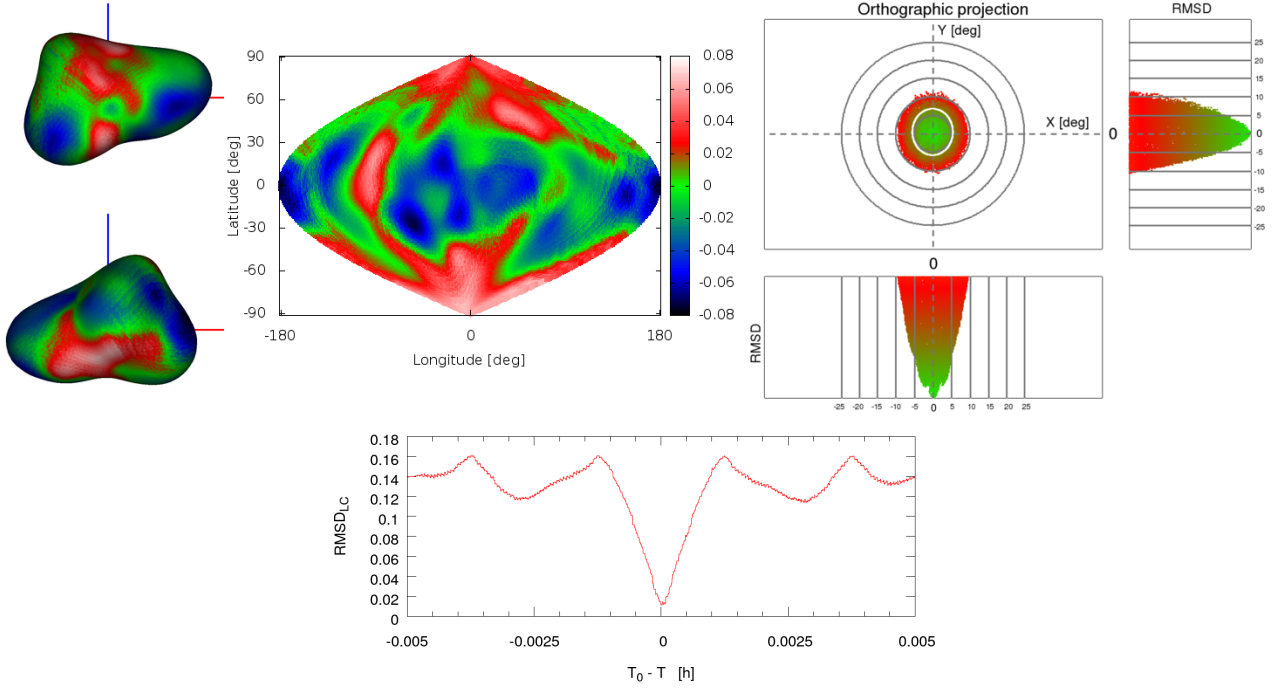


Figure A3. Topography and pole solution maps with periodogram for model A, $\beta = 45^\circ$, phase angles 0° , 14° , 16° , all apparitions.

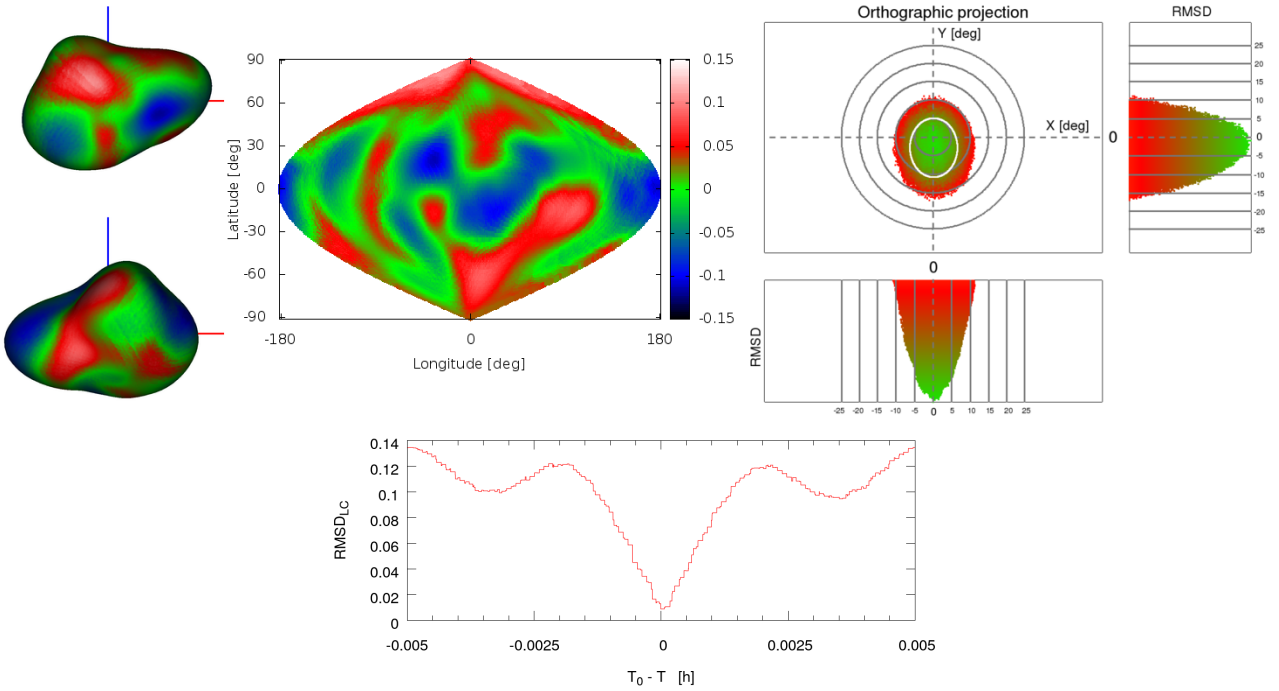


Figure A4. Topography and pole solution maps with periodogram for model A, $\beta = 0^\circ$, phase angles 0° , 14° , 16° , 1234 apparitions.

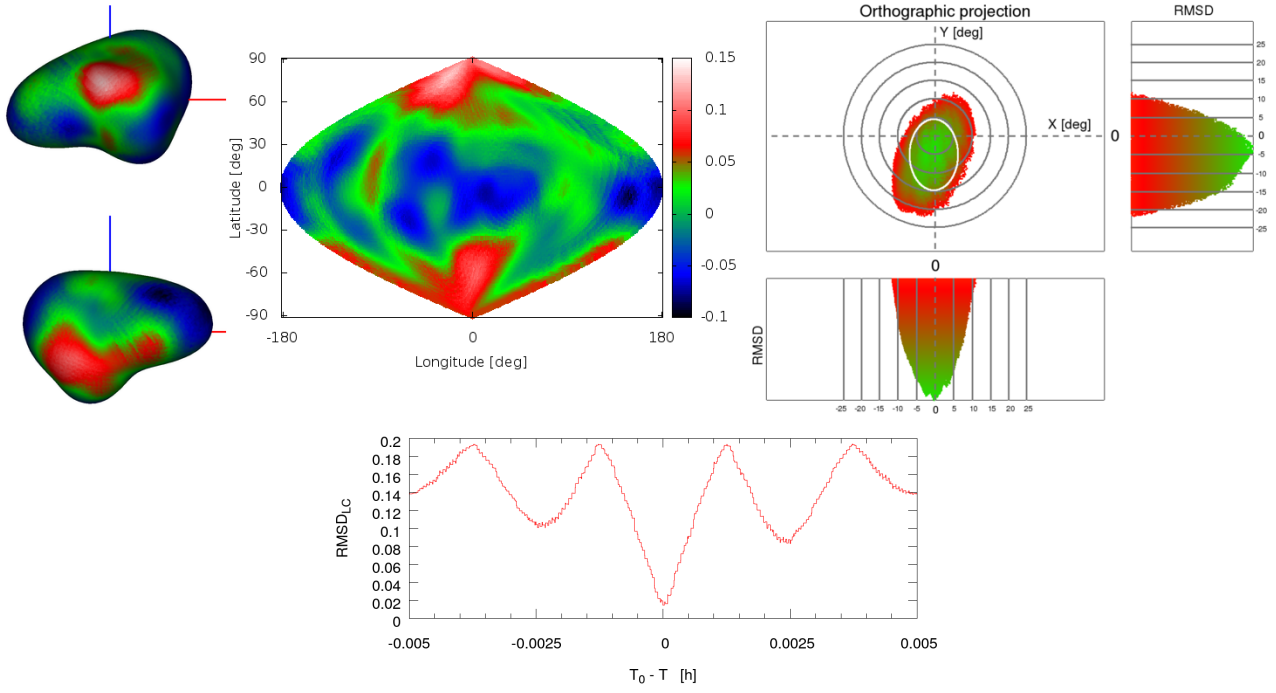


Figure A5. Topography and pole solution maps with periodogram for model A, $\beta = 45^\circ$, phase angles $0^\circ, 14^\circ, 16^\circ$, 1256 apparitions.

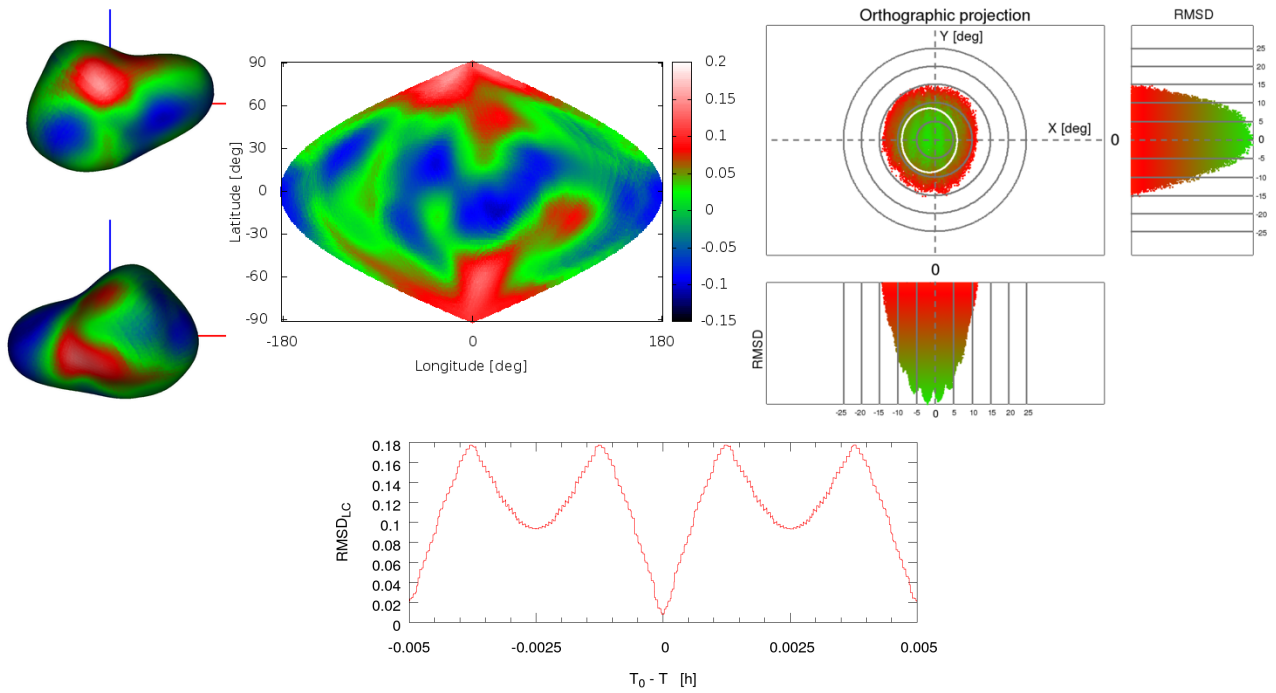


Figure A6. Topography and pole solution maps with periodogram for model A, $\beta = 45^\circ$, phase angles $0^\circ, 14^\circ, 16^\circ$, 1357 apparitions.

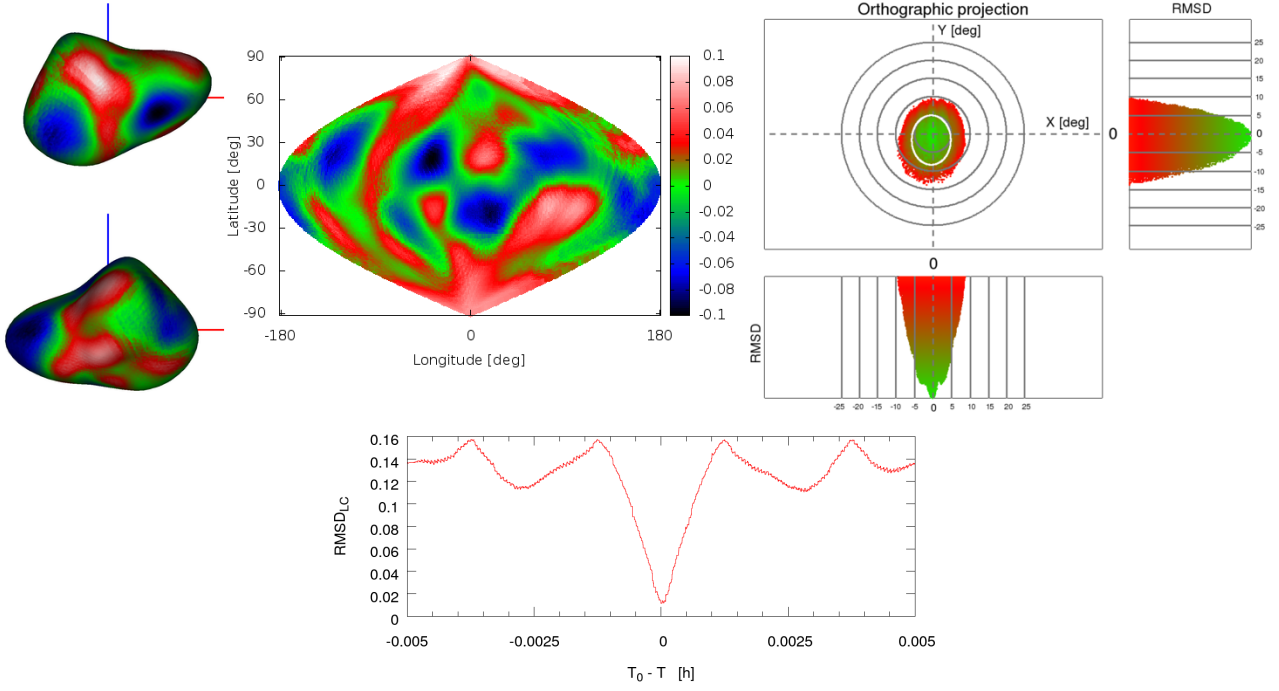


Figure A7. Topography and pole solution maps with periodogram for model A, $\beta = 45^\circ$, phase angles 0° , 14° , all apparitions.

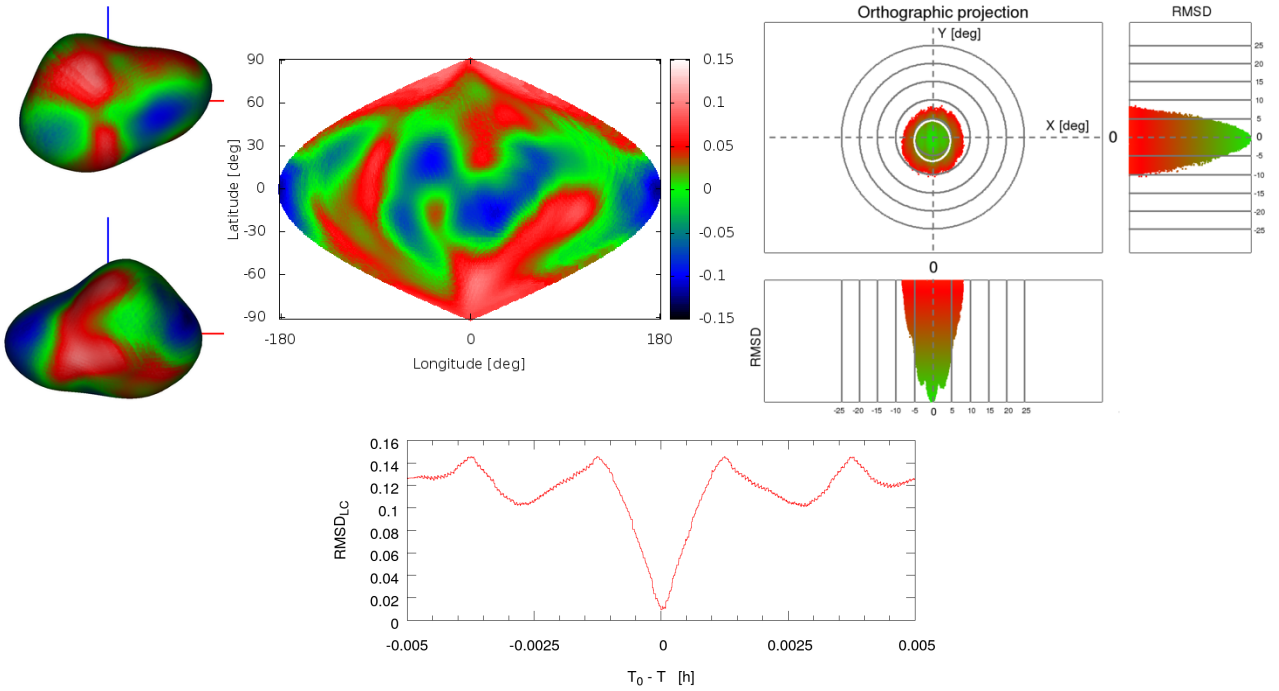


Figure A8. Topography and pole solution maps with periodogram for model A, $\beta = 45^\circ$, phase angles 0° , all apparitions.

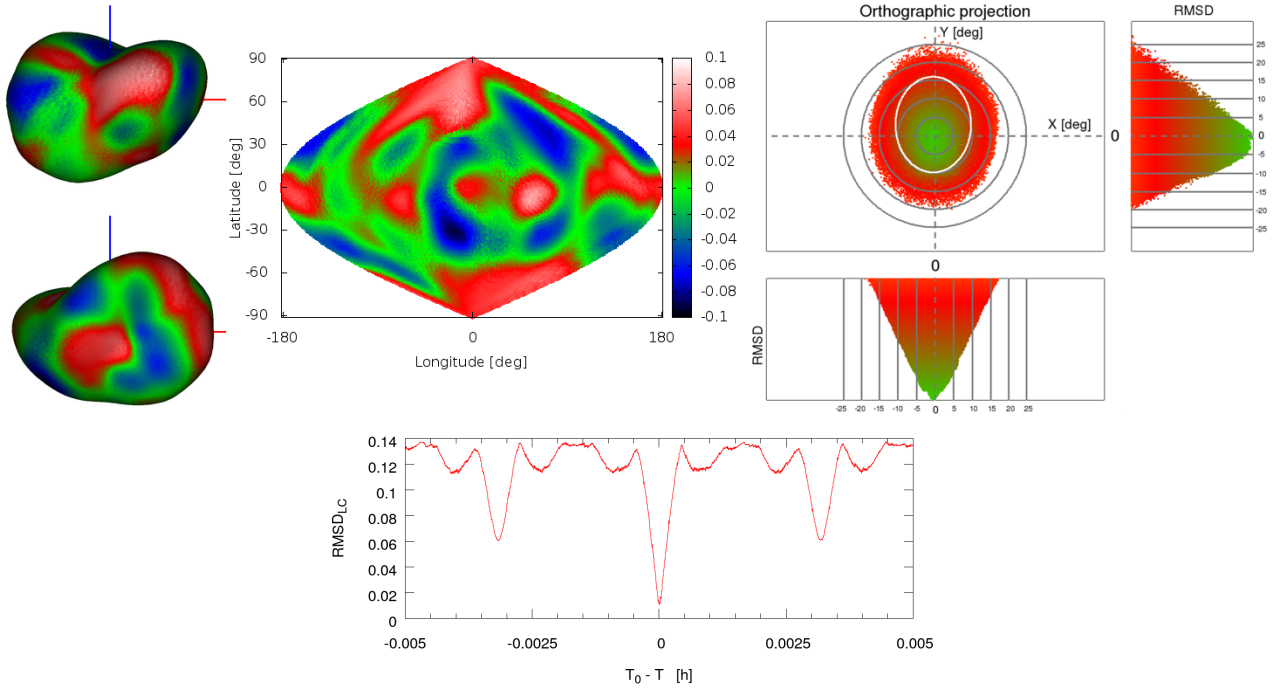


Figure B1. Topography and pole solution maps with periodogram for model B.

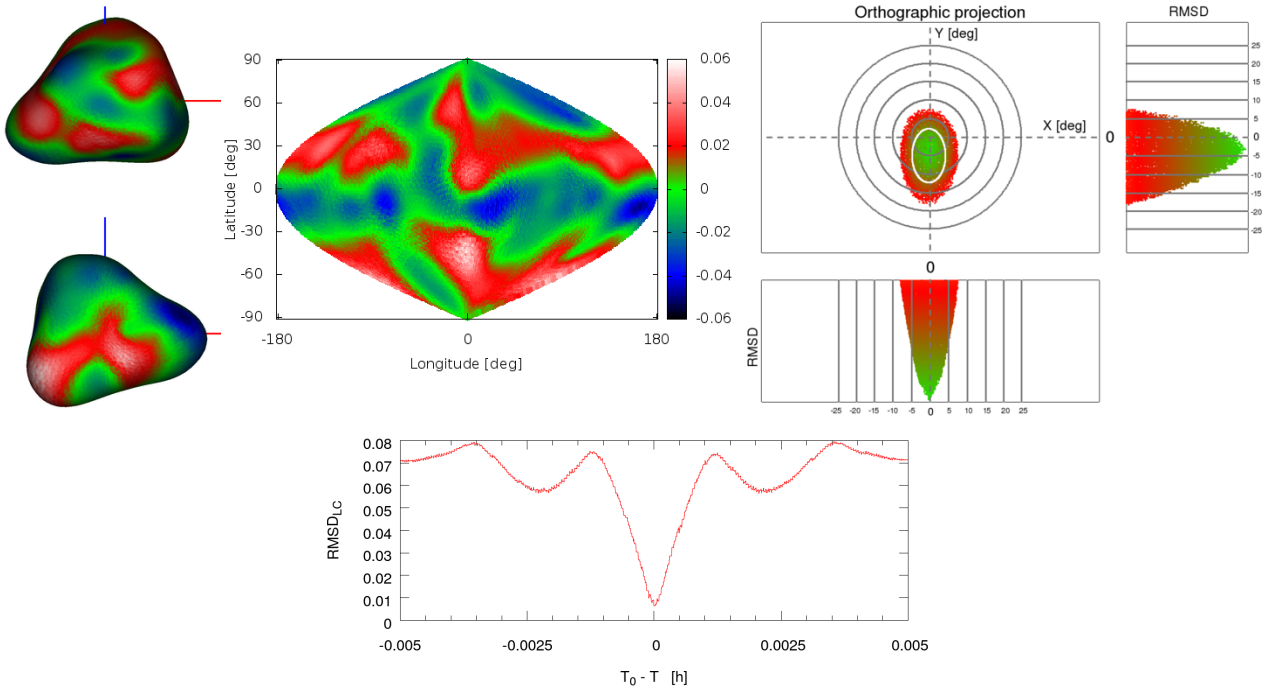


Figure B2. Topography and pole solution maps with periodogram for model C.

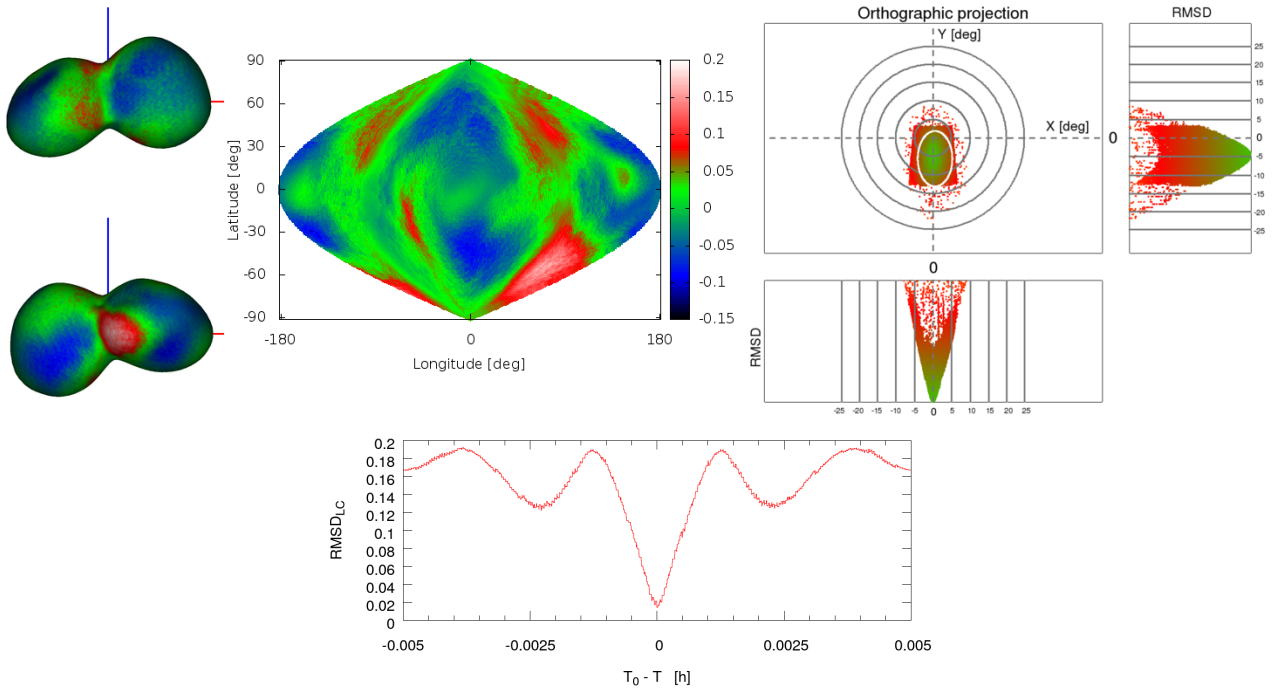


Figure B3. Topography and pole solution maps with periodogram for model D.

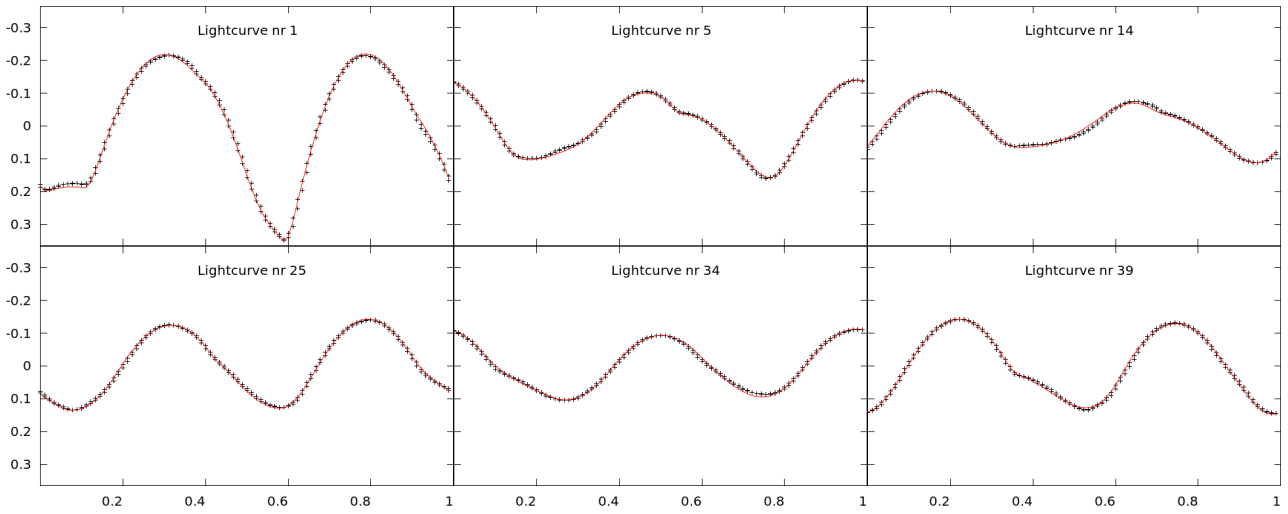


Figure C1. Some of the model A lightcurves.

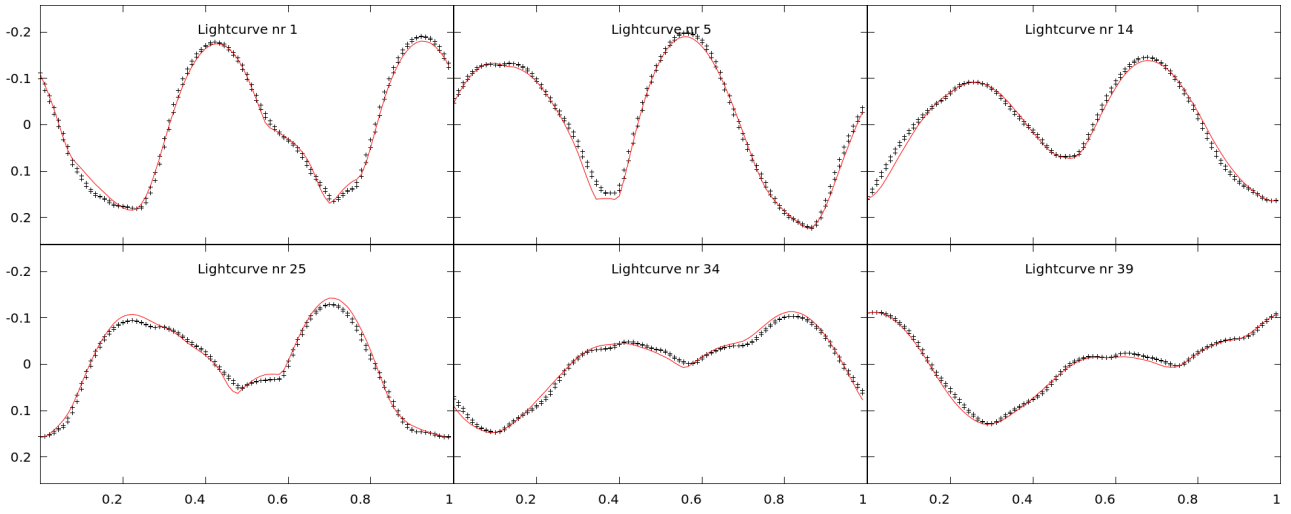


Figure C2. Some of the model B lightcurves.

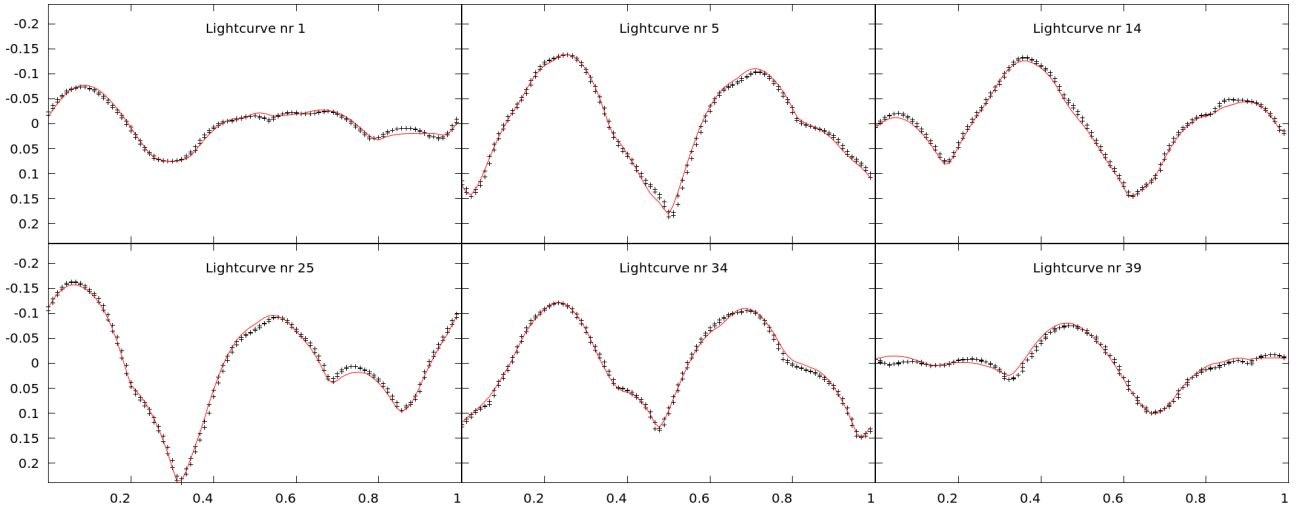


Figure C3. Some of the model C lightcurves.

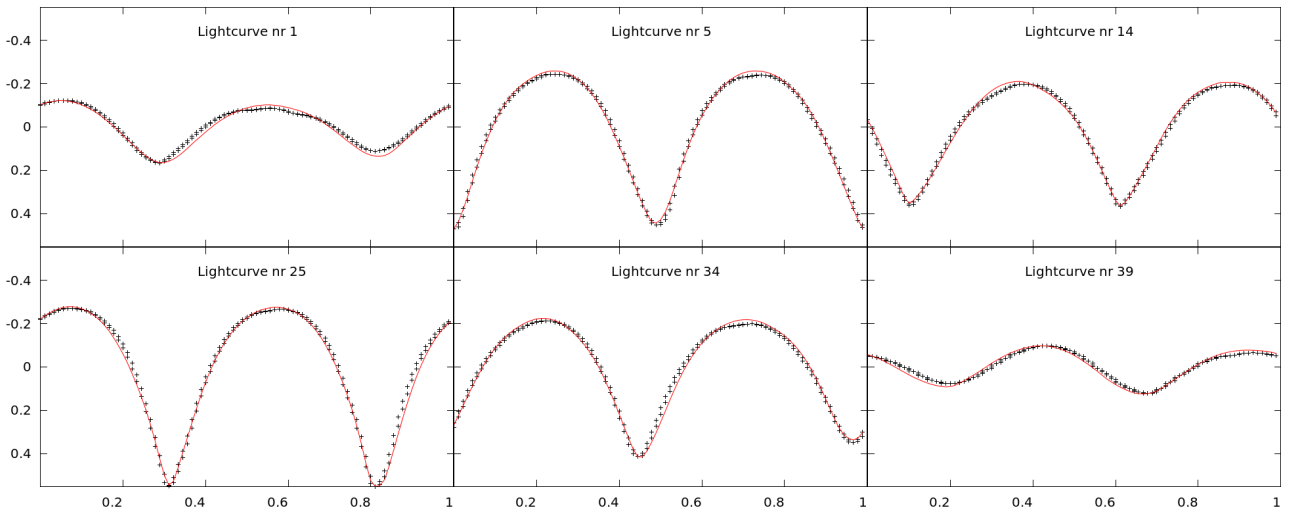
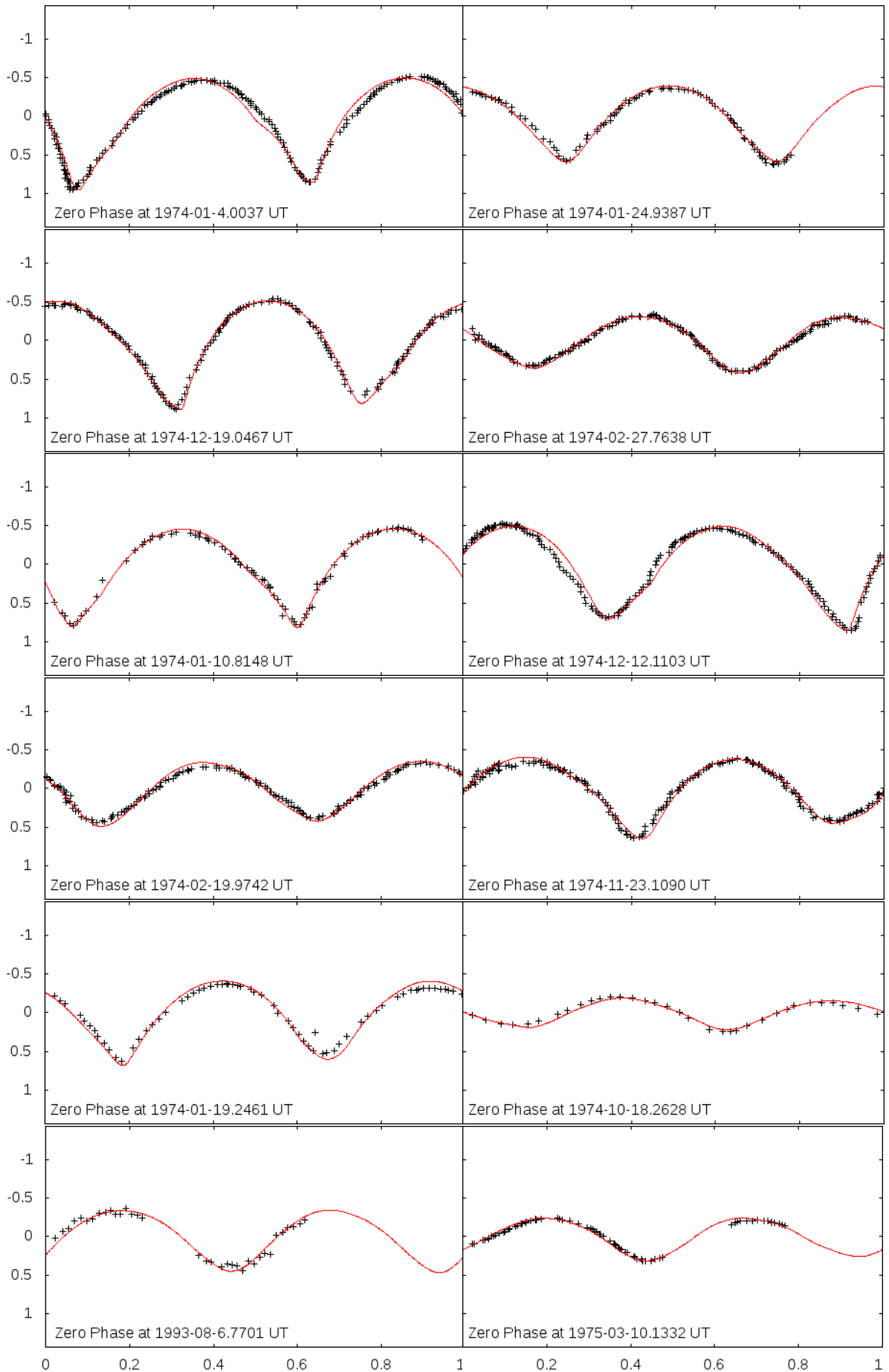


Figure C4. Some of the model D lightcurves.



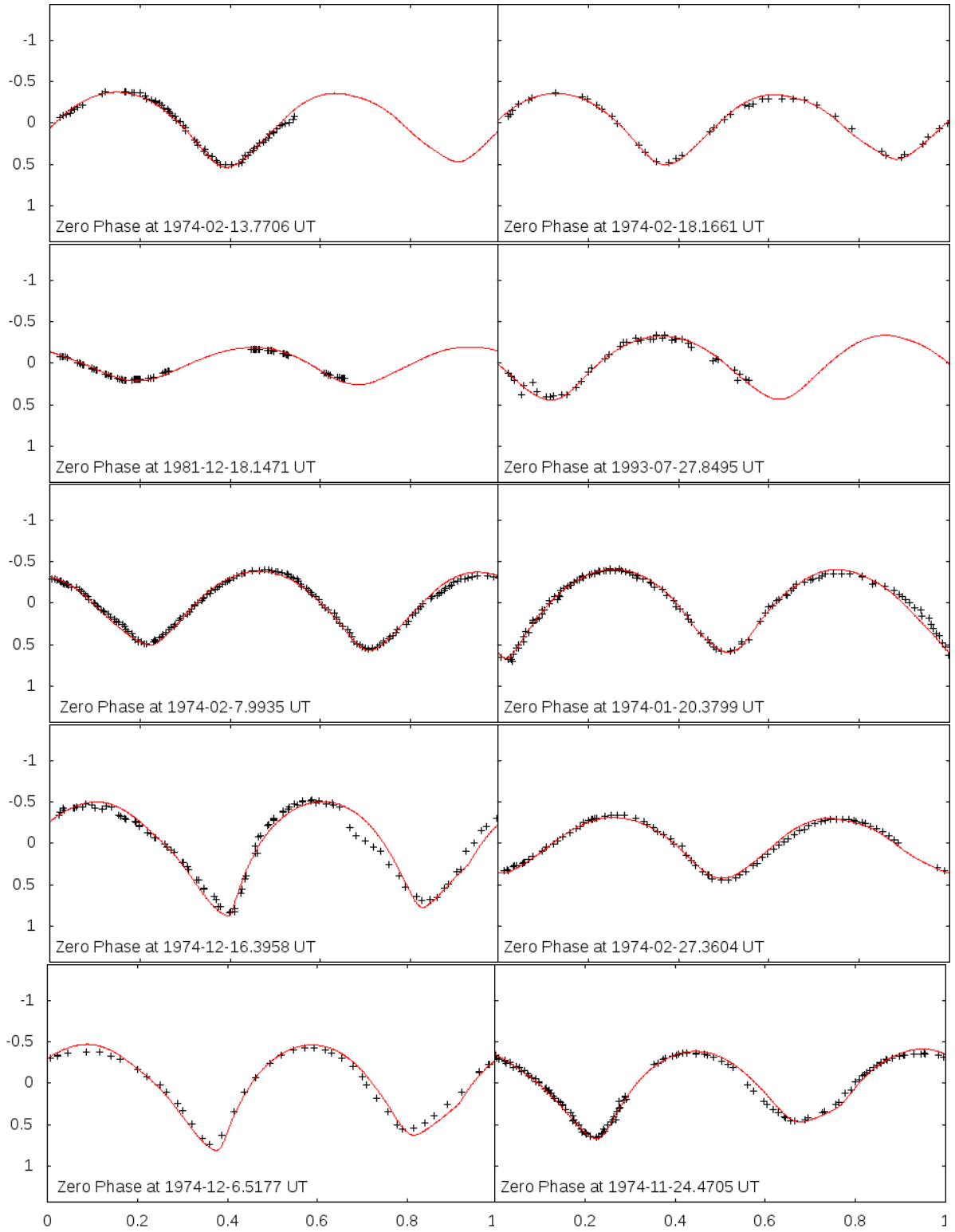
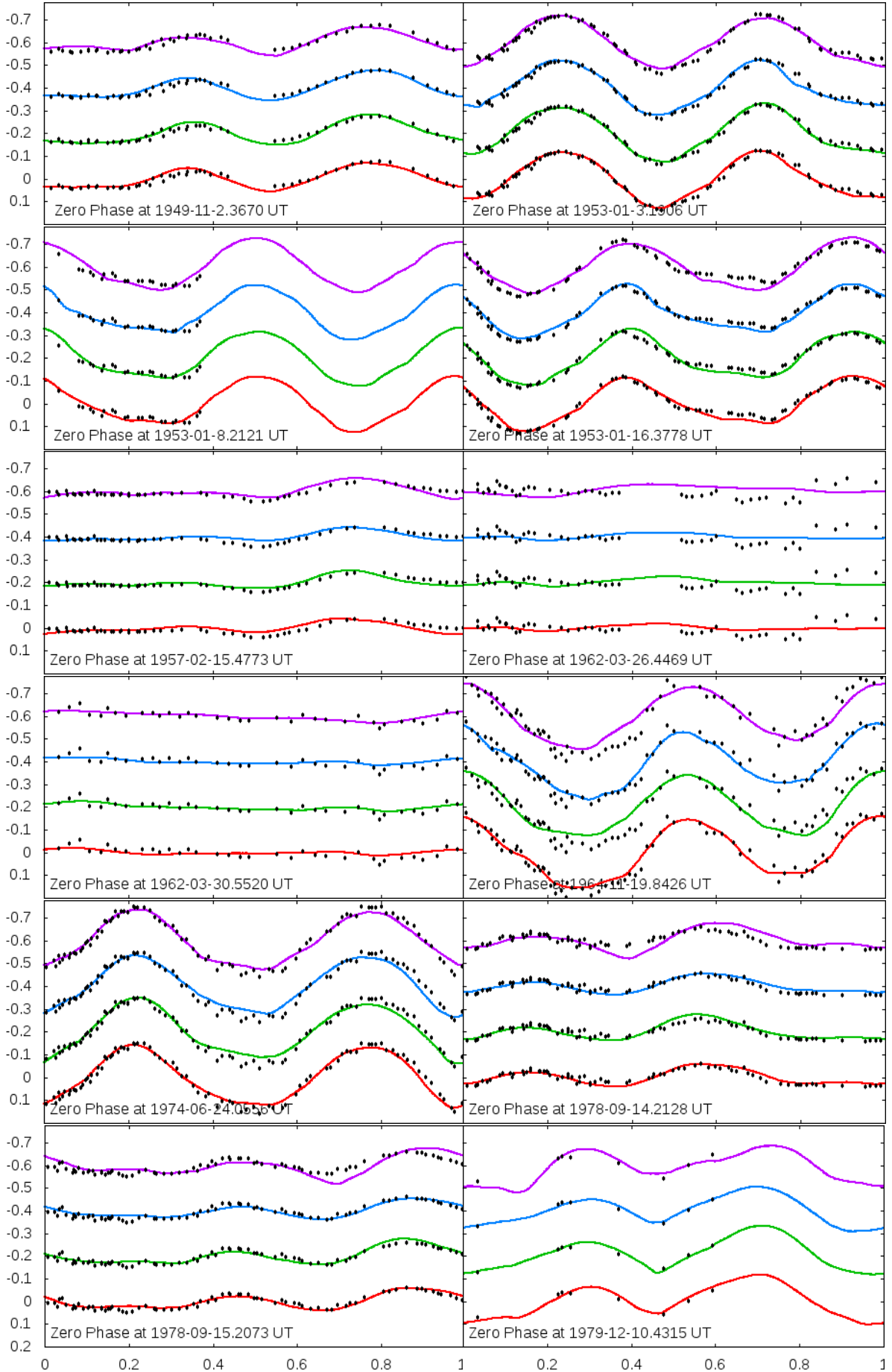


Figure D1. Some of the (433) Eros lightcurves (black points) vs. Eros model (red line).



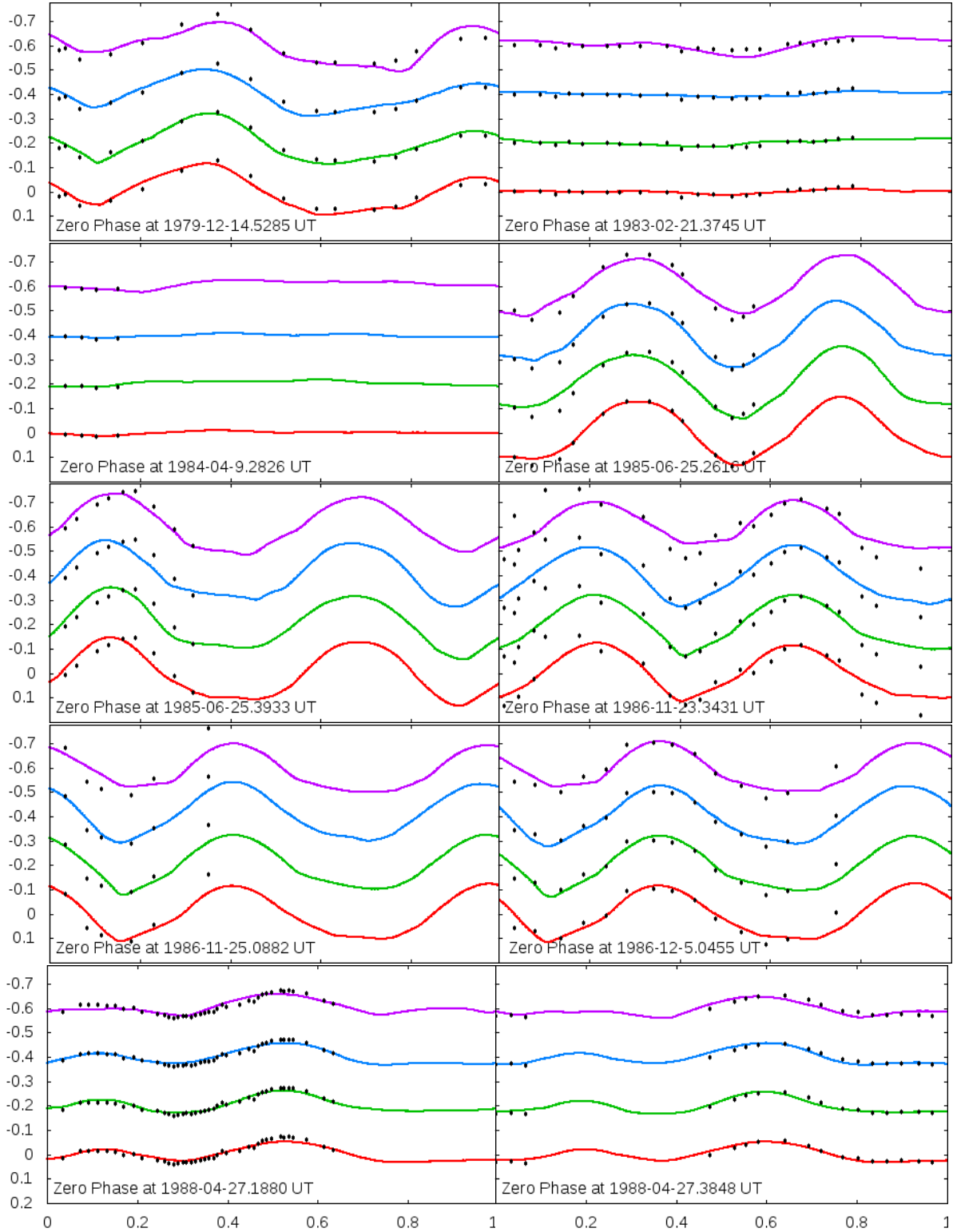


Figure E1. Some of the (9) Metis lightcurves (black points) vs. various Metis models. First from the top (violet): KOALA (Hanus et al. 2013), second from the top (blue): convex model (Torppa et al. 2003), third from the top (green): ADAM (Viikinkoski et al. 2015), bottom (red): SAGE (this work).